



A revised core-seismic integration in the Molloy Basin (ODP Site 909): Implications for the history of ice rafting and ocean circulation in the Atlantic-Arctic gateway

Jens Gruetzner^{*}, Jens Matthiessen, Wolfram H. Geissler, A. Catalina Gebhardt, Michael Schreck¹

Alfred-Wegener-Institut Helmholtz-Zentrum für Polar- und Meeresforschung, Bremerhaven, Germany

ARTICLE INFO

Editor: Dr. Alan Haywood

Keywords:

Fram Strait
Arctic Ocean
Seismic reflections
Ocean Circulation
Stratigraphy
Neogene
ODP Site 909

ABSTRACT

Today's cryosphere reflects an extreme climate state that developed through stepwise global Cenozoic cooling. In this context the opening of the Fram Strait, the Atlantic-Arctic Gateway (AAG), enabled deep-water exchange between the northern North Atlantic and the Arctic Ocean and thereby influenced global ocean circulation and climate.

Here we present a new age model for Ocean Drilling Program Site 909 located in the Molloy Basin, a key site to investigate the late opening phase of the central Fram Strait and the early history of oceanic circulation in the AAG. Our results are based on a revised magnetostratigraphy calibrated by new palynomorph bioevents, which shifts previously used stratigraphies for Site 909 to significantly younger ages in the time interval from c. 15 Ma to 3 Ma. The revised late Miocene to present chronology combined with an improved core-log-seismic integration leads to a new high-resolution seismic stratigraphy for the central Fram Strait that allows a more comprehensive correlation with seismic markers from the western Barents Sea margin and also the adjacent Yermak Plateau. The new stratigraphy implies that prominent maxima in coarse sand particles and kaolinite, often interpreted as evidence for ice rafting in the Fram Strait occur at c. 10.8 Ma, c. 3 Myr later as previously inferred and thus well after the Middle Miocene Climate Transition (c. 15–13 Ma). In the late Tortonian (<7.5 Ma), sediment transport became current controlled, mainly through a western, recirculating branch of the West Spitsbergen Current. This transport was strongly enhanced between c. 6.4 and 4.6 Ma and likely linked to the subsiding Hovgaard (Hovgård) Ridge and the widening of the AAG.

Late Pliocene to Pleistocene seismic reflectors correlate with episodes of elevated ice-rafted detritus input related to major steps in Northern Hemisphere ice sheet growth such as the prominent glacial inception MIS M2 that predates the mid-Piacenzian Warm Period and the intensification of Northern Hemisphere glaciation starting at c. 2.7 Ma. At the beginning of the Mid Pleistocene Transition (c. 1.2–0.8 Ma), sediment accumulation in the Fram Strait significantly decreased.

1. Introduction

The important role of the Arctic Ocean in the modern and Neogene climate system is undisputed and there is increasing awareness that global warming will lead to fundamental changes in the Arctic cryosphere (Briner et al., 2020; Serreze and Barry, 2011). It is known that during large parts of its Cenozoic history the Arctic Ocean was isolated from any global thermohaline circulation system (Jakobsson et al.,

2007). This gradually changed when Greenland and Svalbard started to move apart from each other initiating the opening of the Atlantic-Arctic Gateway (AAG). During the opening an evolving system of fracture zones and mid-ocean ridges changed the global ocean current circulation system, and consequently enabled an exchange of warm Atlantic and cold Arctic water masses (Engen et al., 2008 and references therein; Rudels et al., 2015).

Based on Deep Sea Drilling Project (DSDP) and Ocean Drilling

^{*} Corresponding author.

E-mail address: jens.gruetzner@awi.de (J. Gruetzner).

¹ Now at UKA Cottbus Projektentwicklung GmbH & Co. KG, Cottbus.

Program (ODP) campaigns (Legs 38, 104, 151, 162), and with the help of geophysical datasets, knowledge on the tectonic evolution of the northeast Atlantic basins and continental margins increased (e.g. Stein, 2019; Talwani and Eldholm, 1977; Thiede et al., 1998). However, clarification of the Arctic's role in global climate during the past is often hampered by equivocal stratigraphic constraints and crucial issues like the exact timing of tectonic phases and stratigraphic events. How these phases and events translate into seismic reflection stratigraphy is still a matter of debate. Seismic studies have revealed that sedimentation in the Fram Strait became influenced by contour and bottom currents in the middle to late Neogene (e.g. Eiken and Hinz, 1993; Geissler et al., 2011; Mattingsdal et al., 2014). But there are still large uncertainties about the actual initiation of these current activities and their relation to tectonic processes in the AAG.

Here we present a new, high resolution seismic stratigraphy for the Molloy Basin (central Fram Strait, Fig. 1) that is based on a revised chronology for ODP Site 909 and on a seismic reflection pattern that is better resolved than in previous studies (e.g. Berger and Jokat, 2009). The chronology uses newly identified palynomorph bioevents (Fig. 2) for a revision of the magnetostratigraphy at Site 909 (Fig. 3). As implications of the new chronology this study (i) identifies the paleoceanographic significance of prominent sedimentary changes associated with seismic reflectors in the AAG and (ii) reinterprets previously published proxy records in relation to changes in bottom current controlled sedimentation and ice rafting.

2. Setting

2.1. Tectonic evolution

During the early Neogene, the Arctic Ocean changed from a poorly oxygenated isolated basin to a fully ventilated ocean, which was most likely a result of widening and deepening of the Fram Strait (Jakobsson et al., 2007), the only deep-water gateway from the Arctic Ocean to the other World's oceans in the early/middle Neogene (Ehlers and Jokat, 2013; Straume et al., 2020). Other shallow gateways, i.e. the Bering Strait and the Canadian Arctic archipelago, were possibly closed until the early Pliocene or even mid Pleistocene (Gladenkov et al., 2002; Hegewald and Jokat, 2013; Verhoeven et al., 2011), and the Barents Sea subsided below sea level not before the mid Pleistocene (e.g. Butt et al., 2002; Zieba et al., 2017).

A distinct seismic unconformity marks the top Oligocene (around 24 Ma) in the central Arctic Ocean. This unconformity was possibly formed when the first shallow-water connection between the North Atlantic and the Arctic Ocean was established, accompanied by a significant sea-level drop in the Arctic Ocean causing erosion (Hegewald and Jokat, 2013). Reflection seismic data from the Yermak Plateau support this interpretation indicating that shallow-water connections between the Arctic Ocean and the North Atlantic existed already in the early Neogene (Geissler et al., 2011), probably from 21 Ma (Jokat et al., 2016). However, an Osmium isotope stratigraphy of the ACEX Site (IODP Expedition 302 "Arctic Coring Expedition") even dates the transition from a lake stage to a full ocean phase in the Arctic Ocean to the early Oligocene (36 Ma) (Poirier and Hillaire-Marcel, 2011) requiring a much earlier shallow water passage.

In the early Miocene, strike-slip movements and later oblique ultra-slow spreading in the AAG started to link the active mid-oceanic rift systems in the Eurasian Basin in the north with those in the Norwegian-Greenland Sea in the south (Fig. 1a). Based on detailed aeromagnetic studies the opening of the Molloy Basin began 20–21 Ma ago (Dumais et al., 2021; Ehlers and Jokat, 2009). At the same time seafloor spreading also started at the northern tip of the Lena Trough, the central deep-water passage of the Fram Strait (Fig. 1b). A full spreading system was finally established in the Lena Trough at 11.6 Ma (Jokat et al., 2016). Paleobathymetric modeling suggests that the Fram Strait was already deeper than 2000 m since at least 17 Ma (Ehlers and Jokat,

2013; Knies and Gaina, 2008; Straume et al., 2020).

There is also increasing evidence that tectonic uplift in the circum-Arctic was a controlling factor for the build-up and stability of glacial ice on the continents (Anell et al., 2009; Fjeldskaar and Amantov, 2018; Japsen et al., 2014; Knies et al., 2014; Solgaard et al., 2013). The last two post-breakup uplift phases were identified on Greenland (Døssing et al., 2016; Solgaard et al., 2013), on the Barents Sea Shelf including the exposed Svalbard archipelago (Dörr et al., 2019; Minakov, 2018), and on other passive continental margins of the northeast Atlantic region (Green and Duddy, 2010). These two phases are inferred to have occurred during the late Miocene and at the Mio-/Pliocene transition and may be considered as possible triggers (Japsen et al., 2014), first for climate-sensitive dynamic glaciations of the late Miocene (c. 7.5 Ma) (Bierman et al., 2016), and later on for the formation of larger ice sheets during the late Pliocene and Pleistocene (Knies et al., 2014).

The Molloy Basin (Fig. 1b) comprises the c. 200 km wide and c. 2.5 km deep Fram Strait Sill south of the Molloy Deep, a short spreading segment, and is bounded by the Hovgaard Ridge towards the south and by the Svyatogor Ridge towards the east. The origin of the Hovgaard Ridge, a c. 100 km long ridge (1.2 km water depth) that has a triangular outline defined by the 2.4 km depth contour (Engen et al., 2008), is not finally resolved. The Hovgaard Ridge was classified as a continental sliver sheared off from the Svalbard margin by Myhre et al. (1982), however, Engen et al. (2008), mainly based on gravity data, concluded that the Hovgaard Ridge likely formed by warping of oceanic crust. The Svyatogor Ridge (Fig. 1b) with a length of 46 km and a width of 5 km is located on the western flank of the Knipovich Ridge on an actively spreading mid-oceanic ridge at the inner junction (inside corner) with the Molloy Transform Fault (Waghorn et al., 2018). Sediments on the elongated Svyatogor Ridge were deposited by contourites, and the presence of a gas hydrate system on the ridge has been documented (Johnson et al., 2015).

2.2. Oceanography

The opening of the AAG was paramount for establishing the modern water-column structure in the Arctic Ocean since it enabled deep-water exchange between the northern North Atlantic and the Arctic Ocean. In the modern ocean, transport of warm and saline waters to northern latitudes occurs via the North Atlantic Current (NAC), an important component of the Atlantic Meridional Overturning Circulation (AMOC). Today, the NAC transports c. 7.5–8.5 Sv ($1 \text{ Sv} = 10^6 \text{ m}^3 \text{ s}^{-1}$) of warm, saline Atlantic waters across the Greenland-Scotland Ridge into the Nordic Seas (Østerhus et al., 2005). Combined with export of Polar Water and sea ice through the Fram Strait this inflow of Atlantic Water, with the majority (90%) flowing east of Iceland, is the dominant heat regulation for the Arctic Ocean (Schauer et al., 2004). Thus, changes in the strength and position of the NAC affect continental ice sheet growth and climate in the Northern Hemisphere. North of the Greenland-Scotland Ridge more than half of this Atlantic inflow continues northward as separate branches of the Norwegian Atlantic Current (Fig. 1a). At the eastern side of the strait relatively warm and saline Atlantic Water is transported northward with the West Spitsbergen Current (WSC). The western baroclinic (i.e., varying with depth) flow follows the Arctic Front through the central Norwegian and Greenland Seas and ultimately converges with the WSC in Fram Strait (Orvik and Nüiler, 2002). At 78°50'N the northward directed long-term mean net volume transport ($6.6 \pm 0.4 \text{ Sv}$) of the WSC delivers $3.0 \pm 0.2 \text{ Sv}$ of water warmer than 2 °C (Beszczynska-Möller et al., 2012).

While some of this Atlantic Water recirculates in the Fram Strait (Beszczynska-Möller et al., 2012) and enters the Molloy Basin (Fig. 1a), the remaining WSC separates into two further branches. The Svalbard branch (Aagaard et al., 1987) flows eastward along the shelf edge of Northern Svalbard and transports the warmest water. Another branch follows the western flank of the Yermak Plateau and turns to the east north of plateau. Due to tidal mixing at the Yermak Plateau this branch

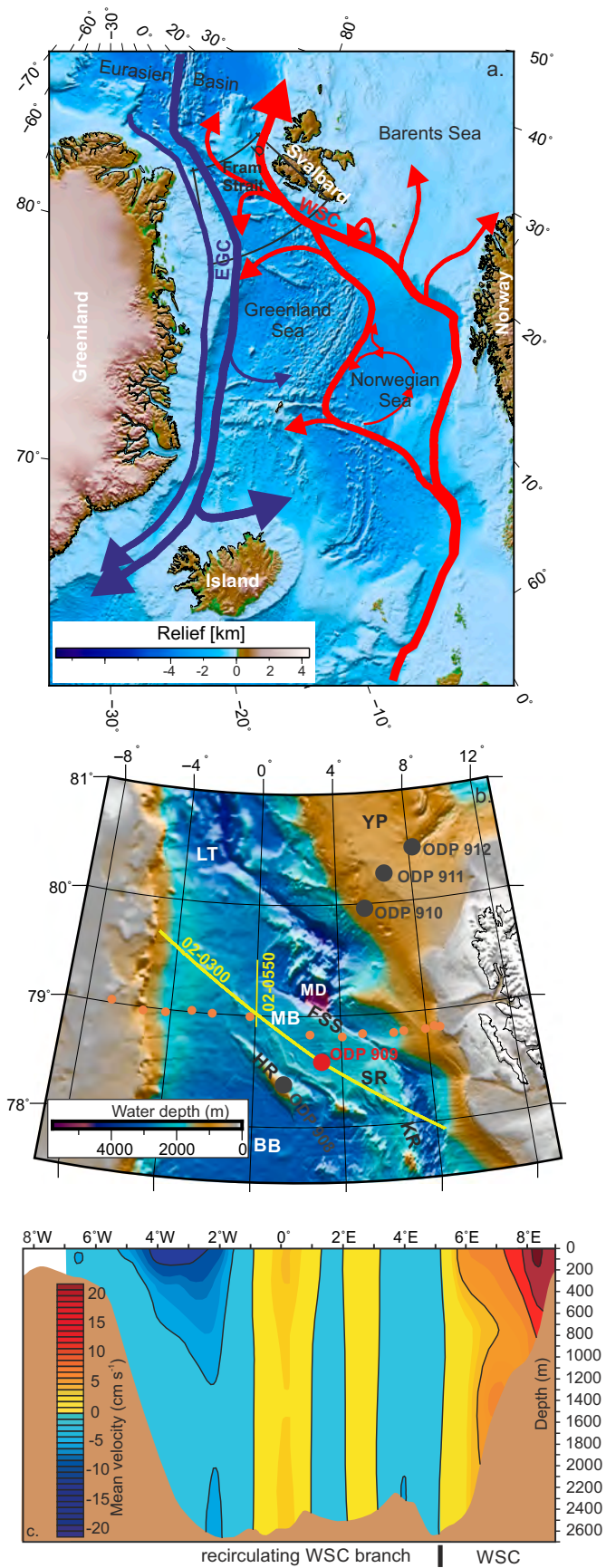


Fig. 1. (a) Circulation scheme for the Nordic Seas and Fram Strait (Beszczynska-Möller et al., 2012), EGC = East Greenland Current, WSC = West Spitsbergen Current. (b) Bathymetry (Jakobsson et al., 2012) of the central Fram Strait area with locations of reflection seismic profiles from Expedition ARK-XVIII/2 (yellow lines), ODP drill sites (big dots) and locations of a moored oceanographic array (small orange dots). Geomorphologic features: LT: Lena Trough, MD: Molloy Deep, MB: Molloy Basin, BB: Boreas Basin, YP: Yermak Plateau, FSS: Fram Strait Sill, HR: Hovgaard Ridge, KR: Knipovich Ridge, SR: Svyatogor Ridge. (c) Mean velocity of (meridional) current component at 79°N derived from the moored section (modified after Beszczynska-Möller et al., 2012). (For interpretation of the references to colour in this figure legend, the reader is referred to the web version of this article.)

loses its Atlantic Water signal and carries less warm water (Saloranta and Haugan, 2001). At the western side of the gateway, low salinity polar surface water as well as cooled Arctic Atlantic Water from the Arctic Ocean is transported south by the East Greenland Current (EGC). In the Fram Strait the EGC is enriched by the recirculating branch of the WSC (Rudels et al., 2015). Evidently, the relative size and strength of the WSC (with its different branches) and the EGC largely determine the net input of oceanic heat to the Arctic Ocean and likely have done so in the past. As such the WSC as the northern extension of the NAC into the cold Arctic should have sensitively reacted to changes in the NAC/AMOC strength, which in turn is related to the opening/closing history of other oceanic gateways like the Greenland-Scotland Ridge (e.g. Uenzelmann-Neben and Gruetzner, 2018), the Bering Strait (e.g. Hu et al., 2007) or the Central American Seaway (Haug and Tiedemann, 1998).

2.3. Ocean Drilling Program (ODP) Site 909

ODP Site 909 (Myhre et al., 1995b) is located in 2519 m water depth on the Greenland-Spitsbergen Sill, a gently elevated area in the Molloy Basin (central Fram Strait) immediately north of Hovgaard Ridge and west of the Svyatogor Ridge (Fig. 1b). Site 909 is a key site to date the late opening phase of the Fram Strait and the early history of the corresponding oceanic current evolution. It was also drilled to document changes in major water mass boundaries and to provide records of the onset and evolution of Arctic glacial history (Myhre et al., 1995b). Three holes were drilled to a maximum depth of 1061.8 m below seafloor (mbsf) reached at Hole 909C. The average recovery rate was 61.9% with strongly decreasing rates below 900 mbsf (Fig. 2). Based on differences in texture, composition, and sedimentary structures the sediment section was subdivided into three main lithologic units (Fig. 2). Heavier hydrocarbons (such as hexane) and an increase in thermogenic hydrocarbon formation were found below 700 mbsf. Drilling eventually had to be terminated because of a drastic two-step increase in heavier hydrocarbon concentrations (C3-C7) at about 1020 and 1050 mbsf.

Initially, the time scale for Site 909 was determined primarily by the identification of magnetic reversals (Myhre et al., 1995b). However, below 90 mbsf paleomagnetic age determinations suffered from incomplete core recovery and core disturbance such that magnetic boundaries (Fig. 3) were difficult to define. The initial report thus already lists two possible stratigraphic models which were modified by postcruise stratigraphic work (Hull et al., 1996; Kaminski et al., 2006; Poulsen et al., 1996). Therefore, later sedimentological studies (Knies and Gaina, 2008; O’Connell et al., 1996; Thiede et al., 1998; Winkler et al., 2002; Wolf-Welling et al., 1996) referred to an updated version of the second of the initial models (Fig. 4), which implies an early Miocene age (>16 Ma) for the base of Hole 909C.

A first correlation of the Site 909 sedimentary units to seismic data was undertaken by Myhre et al. (1995b) but without integrating any age information. Later on Berger and Jokat (2009) used Site 909 to date three seismic units for a regional interpretation of the glacial history along the NE Greenland margin. Depth conversion for that study was based on a velocity model derived from sonobuoy data (Berger and Jokat, 2009). However, this velocity model is not accurate enough to

(caption on next column)

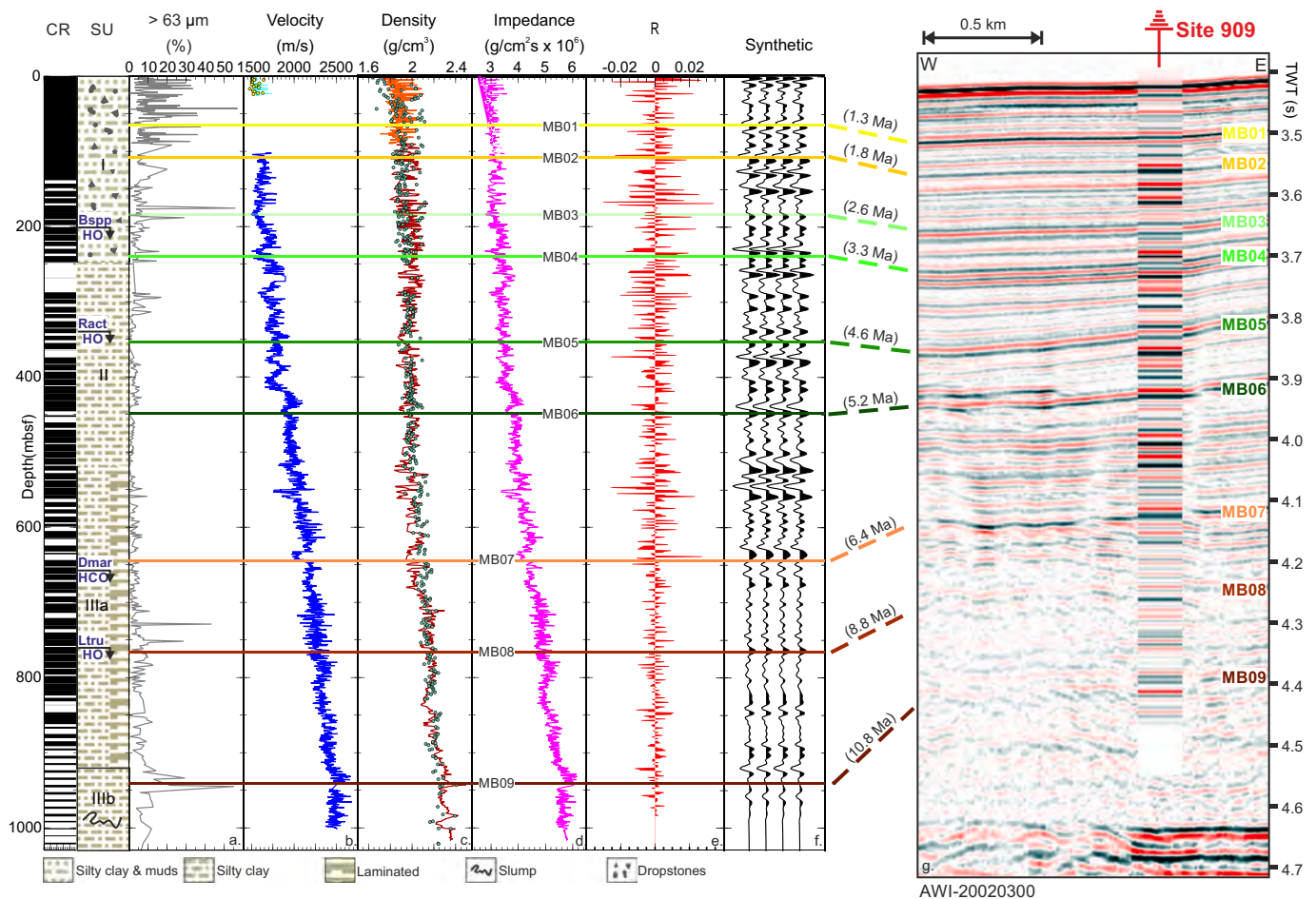


Fig. 2. Sand (> 63 μm) content (a), P-wave velocity (b), bulk density (c), seismic impedance (d), reflection coefficient (e), and synthetic seismogram (f) for ODP Site 909 in comparison to core recovery (CR) and sedimentary units (SU) as defined by Myhre et al. (1995b). Marked on the SU are bioevents used for developing the age model (Bsp = *Barssidinium* spp., Ract = *R. actinocoronata*, Dmar = *D. martinheadii*, Ltru = *L. truncatum*, HO = highest occurrence, HCO = highest common occurrence). Curves in b and c are derived from integration of continuous downhole- (darker colours) and core logging (lighter colours) data and shown in comparison to discrete measurements on sediment samples (dots). To gain a complete velocity profile, a linear interpolation of velocities was made through the data gap between the PWL and SDT measurements. (g) Detail of seismic reflection profile AWI-20020300 at ODP Site 909 (Vertical exaggeration is c. 6). The synthetic seismogram calculated from Site 909 data is overlain. Coloured horizontal lines mark seismic reflectors with assigned ages in Ma (see Table 2 for uncertainty estimations).

gain a detailed integration with ODP Site 909 (see supplementary Fig. 2).

3. Data and methods

3.1. Seismic reflection data

The seismic profiles used in this study were acquired by the Alfred Wegener Institute Helmholtz Centre for Polar and Marine Research (AWI) during expedition ARK XVIII/2 with the vessel RV Polarstern (Jokat, 2003). The seismic energy was generated with a 24 L (8 × 3 L) VLF airgun cluster towed 10 m behind the ship. The shot interval was 15 s, which is equivalent to a shot spacing of 35–40 m. Heavy ice conditions only allowed recording with a 600 m long streamer equipped with 96 active channels resulting in a hydrophone group spacing of 6.25 m. The post-cruise processing sequence of the multichannel seismic data included demultiplexing, editing, common depth point (CDP) sorting, velocity analyses, normal moveout correction, filtering and stacking.

An important profile is the northwest–southeast orientated profile AWI-20020300 (Fig. 1b). This profile is situated in the Molloy Basin north of the Hovgaard Ridge and crosses ODP Site 909 at CDP 5675 in a water depth of 2520 m. For this study we re-processed profile AWI-20020300 and its crossing profile AWI-20020550 with means of

filtering in the f-k domain in order to remove distortions in the uppermost levels below the seafloor that are mainly caused by ghost and bubble signals. This way higher resolution in the uppermost sedimentary section was gained, which allowed much better insight into internal reflection characteristics and subsequently an improved correlation between seismic lines and borehole/core data.

Prominent reflectors of strong to moderate amplitude identified in the seismic profiles were dated using a revised chronology for ODP Site 909 (Table 1). The inferred ages of the upper seven reflectors (Table 2) have uncertainties originating from a possible variability in rate of sediment accumulation between the age control points. We estimated these uncertainties by assuming a ± 50% variability in sedimentation rates, leading to higher age uncertainties for reflectors further away from age control points. For reflectors occurring below the deepest magnetostratigraphic marker at 762.40 mbsf the age span derived from biostratigraphy for the base of Hole 909C was used to calculate average reflector ages and uncertainties. Furthermore, for all reflectors we assumed a seismic depth resolution of ±10 m accounting also for possible mismatches between the core- and log depth scales (see 3.2).

3.2. Physical properties and synthetic seismograms

For this study we make use of physical property records from both,

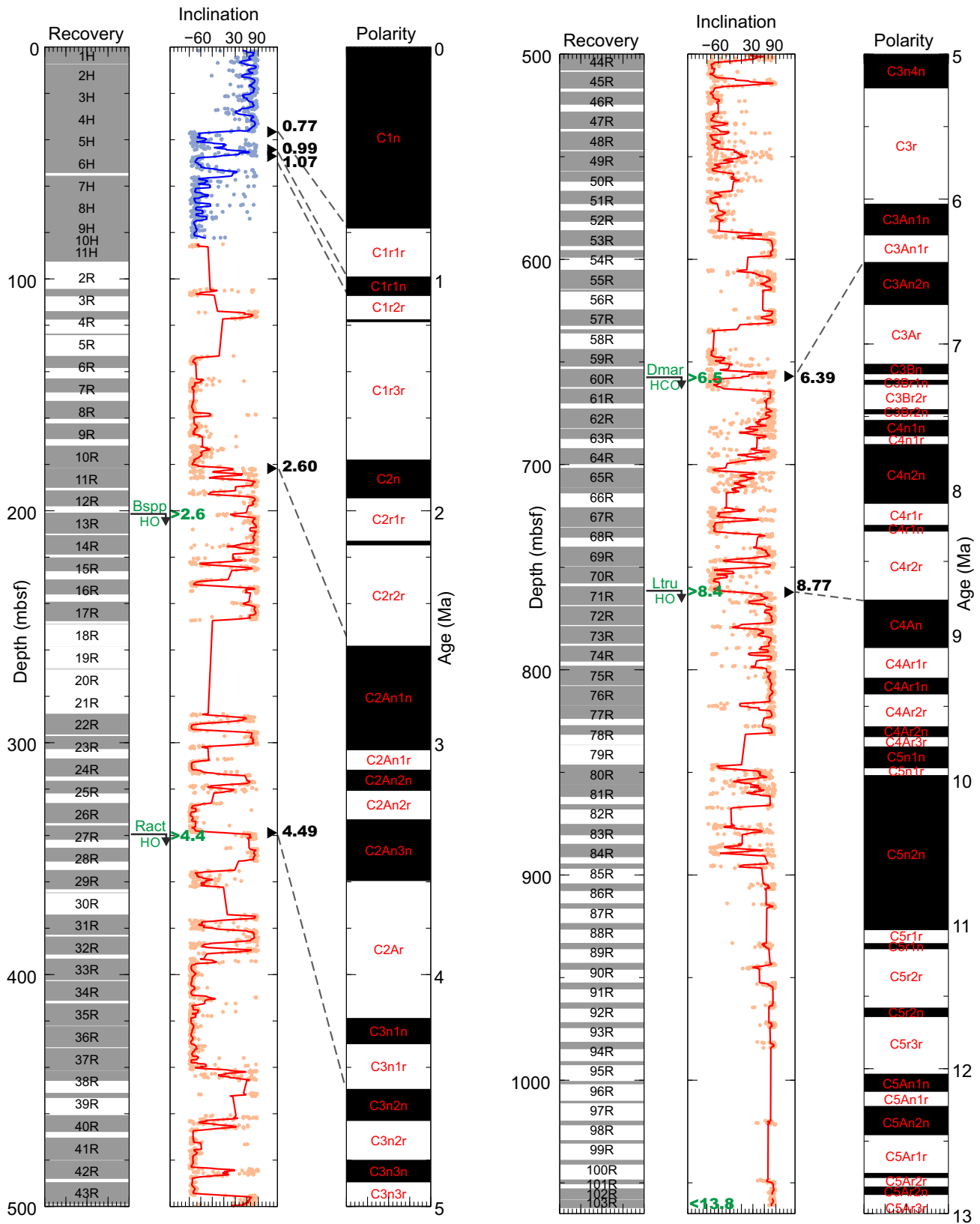


Fig. 3. ODP Site 909 core recovery (left) and inclination of the natural remanent magnetization of holes A (blue) and C (red) versus depth (middle) in comparison to the geomagnetic polarity time scale (right) of Ogg (2020). Dots indicates the inclination after 30 mT demagnetization (Myhre et al., 1995b). Solid lines correspond to 15-point running average. Marked in green are dinoflagellate cyst and acritarch events (Bspdp = *Barssidinium* spp., Ract = *R. actinocoronata*, Dmar = *D. martinheadii*, Ltru = *L. truncatum*, HO = highest occurrence, HCO = highest common occurrence) that were identified in this study and used to constrain magnetostratigraphic age picks (dashed lines, black numbers). All ages in Ma after Gradstein et al. (2020). (For interpretation of the references to colour in this figure legend, the reader is referred to the web version of this article.)

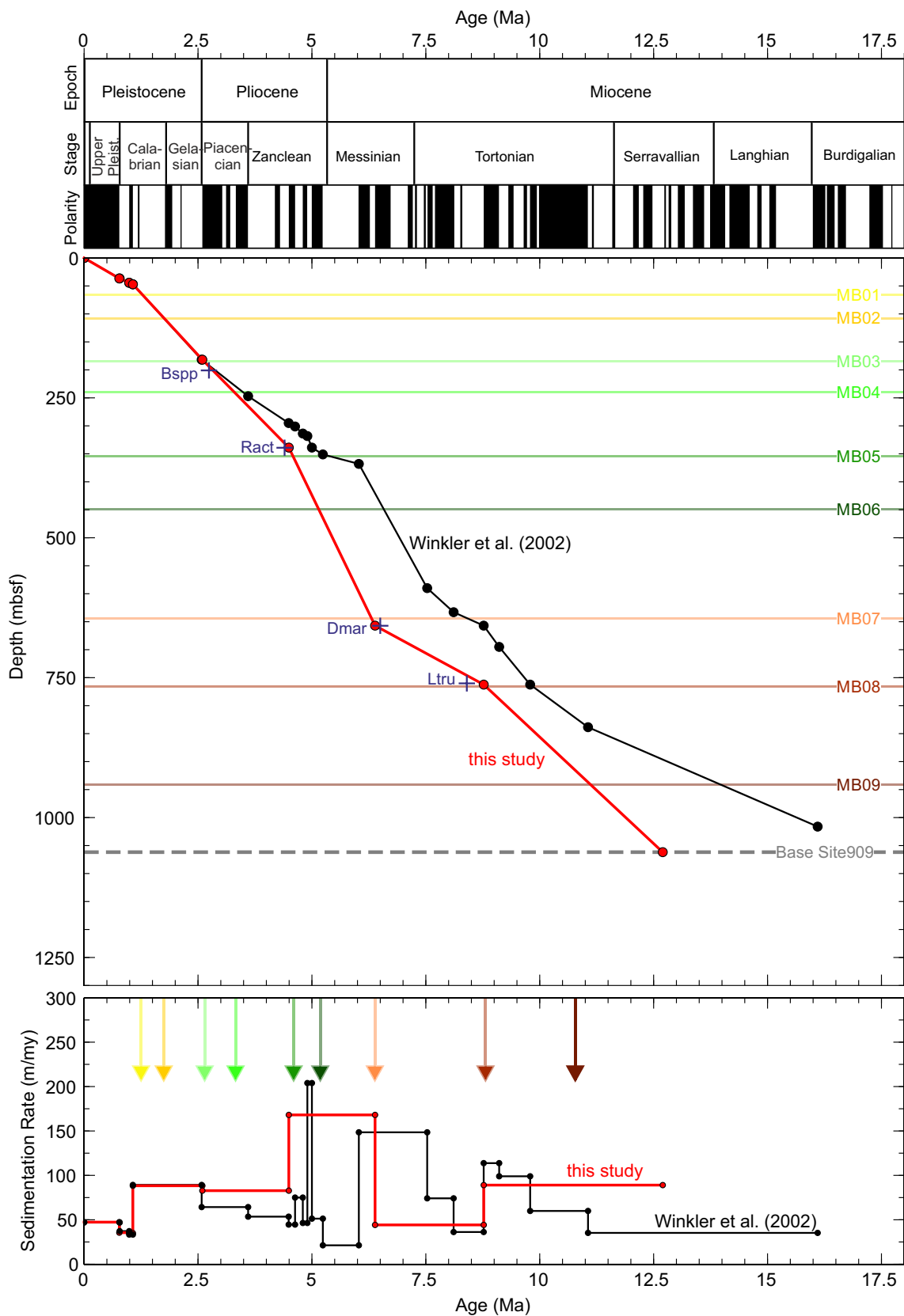


Fig. 4. New age vs. depth (a) and age vs. sedimentation rate (b) relationships for ODP Site 909 (red) in comparison to the previously published age model (black) by Winkler et al. (2002). Coloured lines and arrows mark prominent seismic reflectors identified in line AWI2002-0300. Crosses mark biovents used for developing the age model (Bsp = *Barrisdinium* spp., Ract = *R. actinocoronata*, Dmar = *D. martinheadii*, Ltru = *L. truncatum*). (For interpretation of the references to colour in this figure legend, the reader is referred to the web version of this article.)

Table 1
Age model for Site 909.

Hole-Core Section, Interval	Depth Site 909 (mbsf)	Age (Ma)*	Boundary/Chron	Event
909A-05H1, 60	36.60	0.773	C1n/C1r.1r	Brunhes/Matuyama
909A-05H6, 80	44.30	0.990	C1r.1r/ C1r.1n	Top Jaramillo
909A-06H2, 10	47.10	1.070	C1r.1n/ C1r.2r	Bottom Jaramillo
909C-11R1, 15	181.75	2.595	C2r.2r/ C2An.1n	Matuyama/Gauss
909C-27R3, 15	338.85	4.493	C3n.1r/ C3n.2n	
909C-60R3, 60	657.00	6.386	C3An.1r/ C3An.2n	
909C-71R3, 10	762.40	8.771	C4r.2r/C4An	
Base of Hole 909C	1061.80	> 11.6, <13.8		Biostrat

* (Gradstein et al., 2020)

core and downhole measurements. These data are reported on two different depth scales which can deviate from each other by several meters (Lyle et al., 1996). Wireline logs of ODP Leg 151 are reported using the wireline log matched depth below sea floor (wmsf) depth scale, while core measurements, we use here a composite of Holes 909A, B (0–89.5 mbsf) and C (89.5–1061.8 mbsf), are reported on the meters below sea floor (mbsf) depth scale.

Since Hole 909C was not vertical but instead deviated consistently towards northeast, true vertical depth in the hole was calculated from the deviations measured by the general purpose inclinometry tool of the FMS tool string as suggested by Myhre et al. (1995b). Differences between the cored depth and true vertical depth become significant (>5 m) below 605 mbsf cored depth and the true vertical depth of the base of the hole (1061 mbsf cored depth) is 1023 m (Myhre et al., 1995b).

In order to accurately convert between two-way traveltime (TWT) in the seismic section and depth in the borehole we constructed a high-resolution composite velocity (V) profile from P-wave velocity measurements on cores and from downhole logging following the approaches of Myhre et al. (1995b) and Gruetzner et al. (2019). For the uppermost 26 mbsf we used edited and spliced velocity measurements made with the P-wave logger (PWL) on sediment cores from Holes 909A and 909B (Fig. 2b). Micropores, macroscopic cracks, and drilling disturbance precluded measurement of velocity on recovered core below 26 mbsf (Myhre et al., 1995b). For the interval between 102 and 1000 mbsf downhole logs with the Sonic Digital Tool (SDT, processed post-cruise data) provided detailed continuous in-situ velocity information at Hole 909C. From the composite velocity record a second order equation between two-way-traveltime (s) and depth (mbsf) was derived (supplementary Fig. 2). This equation was used to calculate the depths of reflectors below the termination of Site 909.

Bulk density (ρ_b) data used in this study (Fig. 2c) stem from three different measurement methods used during ODP Leg 151: (1) non-destructive density measurements of whole-round core sections with a gamma-ray attenuation porosity evaluator (GRAPE-density), (2) wet-bulk density as one of the so called index properties (wet-bulk density, dry-bulk density, grain density, water content, porosity, and void ratio) which are determined from measurements of weight (wet and dry) and volume of discrete samples, and (3) densities calculated from phasor induction resistivity downhole logging measurements.

Ideally the in-situ velocities derived from downhole logging would be combined with direct downhole density measurements of similar resolution. However, these data could not be generated at Site 909 because of an instrument failure (Myhre et al., 1995b). Instead, we calculated (see supplementary Fig. 1) porosity and density from the deep phasor induction resistivity downhole log (Archie, 1942). These continuous resistivity derived density data offer a 15 cm measurement

resolution and are in very good agreement with discrete measurements on cored material (Fig. 2c). Subsequently, the linear relationship between wet-bulk density and dry-bulk density was used to derive a continuous record of dry bulk densities for the calculation of mass accumulation rates.

P-wave velocity and density data were used to calculate acoustic impedance ($I=V * \rho_b$) and reflection coefficients ($R = (I_2 - I_1 / I_2 + I_1)$) for Site 909 (Fig. 2d, e). Synthetic seismograms (Fig. 2f) are the results of a convolution of these reflection coefficients with an artificial wavelet. We tested Ricker wavelets in the frequency range between 20 and 150 Hz, as well as a zero-phase wavelet extracted from the seismic data. The convolution of the reflectivity series with the data extracted band pass (20–80 Hz) filtered wavelet correlated best with the seismic data and therefore was used to generate the synthetic seismograms.

3.3. Sampling and palynological methods

To improve the chronostratigraphy of Hole 909C, 114 samples (c. 15cm³) were scanned for biostratigraphically useful palynomorphs below 181 mbsf (supplementary Table 1). Sample spacing varied between c. 1 and 10 m depending on preservation of the core material and sedimentation rate as calculated from the age model of Winkler et al. (2002) to obtain a temporal resolution of 100 ka. No samples were studied between 246 and 287 mbsf because of very low recovery. Samples were freeze-dried, weighed, and processed using standard palynological techniques, including treatment with cold HCl (10%) and cold HF (38–40%), but without oxidation or alkali treatments. After each acid treatment the residue was neutralized with demineralized H₂O and sieved over a 6 μ m polyester gaze. Two *Lycopodium clavatum* tablets (Batch no. 124961, X = 12,542, s = \pm 416 per tablet) were added to each sample during HCl treatment to calculate palynomorph concentrations (Stockmarr, 1971). The residue was mounted on microscope slides with glycerine jelly and the coverslips were sealed with non-caking paraffin wax. All slides are stored at the Alfred Wegener Institute Helmholtz Centre for Polar and Marine Research, Bremerhaven, Germany. One slide was completely scanned under a Zeiss Axioskop microscope at 40 \times magnification to record stratigraphically useful dinoflagellate cysts and acritarchs. These initial observations revealed that only few taxa have a consistent stratigraphic range in Hole 909C, and abundances of these selected taxa were visually estimated. Taxonomic nomenclature follows Fensome et al. (2019). The full names of taxa and abundance estimates are listed in supplementary Table 1. As Poulsen et al. (1996) already stated, samples from Hole 909C are flooded by terrestrial organic matter and marine palynomorphs are rare in most samples. Since variable numbers of marine palynomorphs were observed, the abundances are only classified as rare, common, and abundant. Ages are given according to Gradstein et al. (2020).

3.4. Sedimentological data

For this study we re-interpreted grain size measurements (O'Connell et al., 1996; Wolf-Welling et al., 1996), coarse-fraction grain analysis (Wolf-Welling et al., 1996), and clay mineralogy data (Winkler et al., 2002) generated for ODP Sites 908 and 909.

From the grain size measurements, the total coarse fraction (>63 μ m wt%) and the >250 μ m (wt%) fraction were used. The >63 μ m fraction (Fig. 2a) is an effective parameter in controlling P-wave velocity changes in marine sediments, because high concentrations of sand strongly increase the elastic rigidity (μ) of the sediment (Morton, 1975) and a positive relationship between sand content and P-wave velocity has often been reported (e.g. Bassinot, 1993; Breitzke, 2006; Gruetzner et al., 1997). The deposition of coarse-grained material >250 μ m (coarse-sand-, very-coarse-sand-, gravel- and pebble-sized particles) is mainly restricted to iceberg transport (Stein, 2008 for review) and thus can be used to distinguish from transport by sea ice and ocean currents which is dominated by silt, clay and fine sand (63–125 μ m) components

Table 2
Major seismic reflectors of the Molloy Basin.

Horizon	TWT (ms)	TWT (ms bsf)	True Vertical Depth (m)	Depth in Borehole (mbsf)	Age (Ma)	Estimated Age uncertainty (Ma)
Seafloor	3430	0	0.00	0.00	0.0	
MB01	3512	82	65.46	65.46	1.3	± 0.1
MB02	3564	134	107.80	107.80	1.8	± 0.4
MB03	3652	222	183.98	183.99	2.6	± 0.1
MB04	3714	284	239.88	239.94	3.3	± 0.4
MB05	3836	406	353.12	353.65	4.6	± 0.1
MB06	3934	504	447.16	448.69	5.2	± 0.3
MB07	4130	700	637.83	644.16	6.4	± 0.1
MB08	4254	824	754.28	766.17	8.8	± 0.8
MB09	4410	980	916.53	940.99	10.8	± 0.9
Deep reflectors	4638	1208	1147.81	1228.00	14.7	± 1.3

(e.g. Clark and Hanson, 1983). Based on the weight percentages (wt%) records and the new chronology we also recalculated mass accumulation rates (MAR) for various grain size classes. Furthermore, %silt estimated from smear slides (Myhre et al., 1995b) was used to calculate MAR of silt.

Clay mineralogic measurements as outlined by Winkler et al. (2002) yielded relative percentages of smectite, illite, chlorite, and kaolinite. While chlorite and illite chiefly derive from physical weathering of crystalline and diagenetic sedimentary rocks and occur abundantly in high latitude oceans (Chamley, 2001), smectite and kaolinite occur in minor amounts in Arctic sediments, but have been useful in reconstructions of source areas of sediments (Wahsner et al., 1999). Kaolinite is mainly derived from chemical weathering under intense warm, humid conditions which could be excluded for the last 14 Ma in the central Fram Strait. Thus kaolinite in the Molloy Basin is rather an indicator of kaolinite-rich continental source rocks of the fine sediment fraction (Knies et al., 2002). Smectite also dominates in the sediments if chemical weathering was the dominant clay producing process in the source areas, however smectite may as well have been formed by alteration of volcanic rocks (Chamley, 2001).

4. Results

4.1. Palynostratigraphy

The palynostratigraphy is based on species that have relatively robust datums in Neogene sediments in the northern North Atlantic and the Nordic Seas (De Schepper et al., 2017; De Schepper and Head, 2008; Schreck et al., 2012). The stratigraphic ranges of these taxa are compared with those described by Poulsen et al. (1996) in an initial palynostratigraphic study on Hole 909C. Poulsen et al. (1996) studied mainly core catcher samples between Core 27R-CC (341.70 mbsf) and 103R-CC (1062.13 mbsf) of earliest Pliocene and Miocene age. This study uses additional core samples and extends the depth interval upward to the base of the Quaternary (Sample 11R1, 24–26, 181.84 mbsf) according to the magnetostratigraphic interpretations (Myhre et al., 1995b).

Other stratigraphically important species previously reported by Poulsen et al. (1996) such as *Palaecystodinium golzowense* and *Cordosphaeridium minnum* occur only sporadically in low numbers. The comparison of their stratigraphic ranges with those in the compilation by Schreck et al. (2012) and with the palynostratigraphic age model of Hole 909C (Poulsen et al., 1996) reveals that specimens must have been reworked into younger sediments. The interpretation of stratigraphic ranges is further complicated by drilling deformation. Caving might have additionally caused downhole displacement of taxa leading to erroneous lowest occurrences. Therefore, the palynostratigraphic interpretation in this study relies on the highest occurrence (HO) of selected taxa that have a rather persistent stratigraphic range in Hole 909C based on the work by (Poulsen et al., 1996) and the new observations (supplementary Table 1). These bioevents (Figs. 2, 3, 4) are used

for an interpretation of the inclination record to define a robust new age model. Their stratigraphic occurrences in relation to the magnetic polarity pattern are shortly described below.

Barssidinium spp. occurs in most samples between 1029.95 mbsf (Sample 909C-99R1, 75–77) and 200.92 mbsf (Sample 909C-13R1,12–14). *Barssidinium graminosum* is the dominant species of the genus which was observed by Poulsen et al. (1996) in a shorter interval between Sample 909-85R-CC (896.77 mbsf) and the top of the studied section in Sample 27R-CC (341.70 mbsf). *Barssidinium pliogenicum* occurs sporadically and counts were combined with those of *B. graminosum*. The HO of *Barssidinium* spp. at 200.92 mbsf is located in the upper part of a long interval with normal polarity (Fig. 3).

Reticulosphaera actinocoronata occurs from the base of Hole 909C (Sample 909–103R-CC, 7–9, 1062.2mbsf; Poulsen et al., 1996, Sample 103R-CC, 1062.13 mbsf) up to Sample 909C-27R3, 44–46 at 339.14 mbsf at the top of an interval with normal polarity (Fig. 3). A single occurrence at 297.86 mbsf is attributed to reworking. This HO is slightly higher than that reported by Poulsen et al. (1996) in Sample 909C-27R-CC (341.70 mbsf) but these authors did not study samples above their HO level.

Decahedrella martinheadii is present from Sample 87R-1, 28–30 at 914.08 mbsf to Sample 909C-57R4, 98–100 at 629.88 mbsf. Two specimens in Sample 909C-99R-1, 75–77 (1029.95 mbsf) are attributed to caving. Poulsen et al. (1996) observed *D. martinheadii* (as *Evittosphaerula* sp.2 of Manum et al. 1989) in a slightly shorter stratigraphic range from Sample 84R-CC (891.11 mbsf) to Sample 60R-CC (662.23 mbsf). In Hole 909C, this species depicts a sharp decrease in abundance shortly before it disappears as was previously observed by Poulsen et al. (1996). Therefore, a highest common occurrence (HCO) is placed in Sample 909C-60R3, 82–84 (657.22 mbsf) immediately below the HO. The HCO is located within an interval with normal polarity (Fig. 3).

Labyrinthodinium truncatum occurs from the base of the hole up to Sample 71R-1, 88.5–90.5 (760.185 mbsf) while Poulsen et al. (1996) only observed this species from Sample 98R-CC (1020.0 mbsf) up to Sample 80R-CC (855.75 mbsf) and reported an isolated occurrence slightly higher in Sample 909C-69R-CC (749 mbsf). The HO is located slightly above a reversal from positive to negative inclinations (Fig. 3).

Operculodinium? eirikianum was recorded by Poulsen et al. (1996) in isolated samples between sections 98R-CC (1020 mbsf) and 44R-CC (505.77 mbsf). In this study, a few specimens of *O.? eirikianum* also occur in the bottom sample at the base of Hole 909C (Sample 103R-CC, 7–9, 1062.2 mbsf).

4.2. Seismic reflectors and facies

Acoustic basement along line AWI-20020300 shows a very rough topography and is not unambiguously identifiable everywhere (Fig. 5a). Below Site 909 the top of a series of short but strong reflectors at 4.638 s

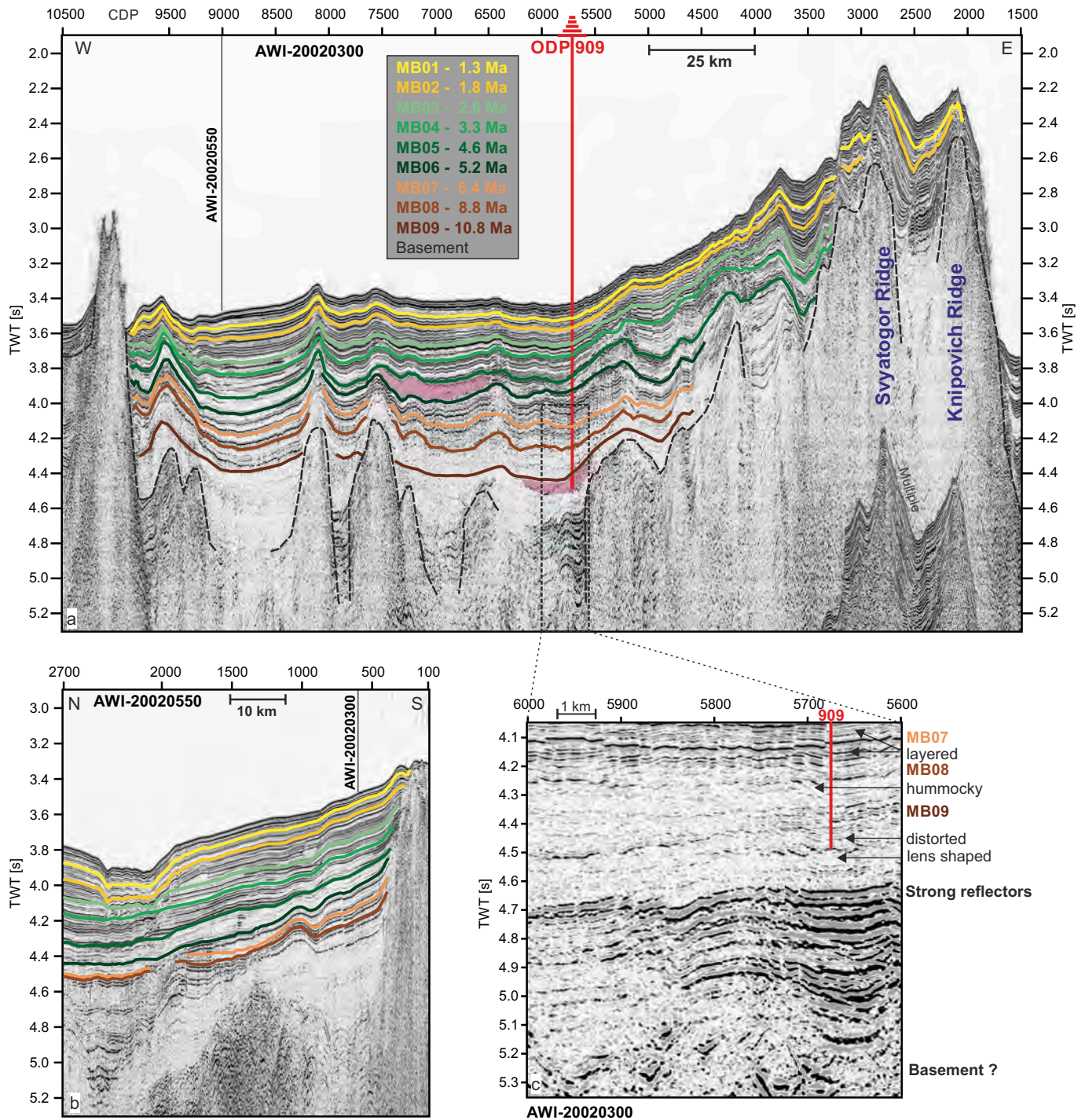


Fig. 5. (a) Time migrated and interpreted section of multichannel seismic reflection profile AWI-20020300 across ODP Site 909 (red vertical line), regional reflectors MB01 to MB09 (Table 2) are traced in brownish (Miocene), greenish (Pliocene) and yellowish (Pleistocene) colours. Dashed black line marks acoustic basement. Magenta areas mark debris lobes. Vertical exaggeration is c. 40. A much less exaggerated (VE c. 7) section of the seismic profile with marked polygonal faults is provided in supplementary Fig. 3. (b) Seismic profile AWI-20020550 crossing at CDP 9007 in south-north direction. (c) Close up of profile AWI-20020300 showing the reflection patterns at the base of Site 909. (For interpretation of the references to colour in this figure legend, the reader is referred to the web version of this article.)

TWT (Fig. 5a, CDPs 5500–6000) was interpreted as acoustic basement in the site survey seismic line BU-20-81² by Myhre et al. (1995b). However,

² We noticed that the seismic figures (Figs. 1 and 43) in the Site 909 initial report chapter (Myhre et al., 1995b) have a mislabeled (shifted) time axis. The correct twt time is the displayed time + 0.5 s.

in line BU-20-81 a sequence of strong hyperbola-like reflectors appears at 1.1 s two-way traveltime (TWT) below sea floor and masks any deeper horizons. From the time migrated section presented in Fig. 5(a, c) and supplementary Fig. 3 we conclude that the reflector at 4.638 s does not represent the top of the oceanic crust, but rather layered deposits on top of a rifted/rotated crustal block. The top of the reflector sequence is calculated to be at c. 1148 mbsf (true vertical depth, Table 2), which is

125 m below the base of Hole 909C (true vertical depth).

Within the sedimentary column of the deep Molloy Basin we identified nine seismic reflectors (MB01 - MB09) of strong to moderate amplitude which are unambiguously correlated with the synthetic record (Table 2, Figs. 2, 5). These seismic reflectors, which can also be traced in the south to north trending Profile AWI-20020550 (Fig. 5b) and likely over a wider area within the Molloy Basin, have been dated according to our new age model (Fig. 4).

The lowermost of these reflectors (MB09, 4.410 s, c. 941 mbsf) is relatively faint and inclined towards the west. The reflector marks a discontinuity roughly at the transition between sedimentary sub-units IIIa and IIIb and forms the top of a transparent, lens shaped package (Fig. 5c) with some weak, discontinuous and inclined internal reflections (Fig. 2g). The sediments recovered from this lithologic section (subunit IIIb, 923.4 to 1061.8 mbsf) comprise laminated intervals of dark gray silty clays, clayey silts, and silty muds interrupted by meter-scale intervals containing slump structures (Myhre et al., 1995b). The slumps exhibit folded and otherwise deformed bedding. At this level, density and velocity increase abruptly (Fig. 6), caused by increased deposition of coarse-grained material (Fig. 6d). Furthermore, a strong enrichment of kaolinite in the fine fraction (Fig. 6g) is observed immediately below MB09.

Between MB09 and MB08 internal reflections are mostly faint and

hummocky in the vicinity of Site 909 (Figs. 2g, 5c). Recovered sediments from this interval (lower subunit IIIa) mostly occur in thin (<5 cm) planar bioturbated beds of very dark greenish gray silty clay and clayey mud (Myhre et al., 1995b).

Reflector MB08 at 4254 ms (766 mbsf, Table 2) is relatively faint, located below two prominent peaks in sand content (Figs. 2 and 6), and corresponds to a moderate upward drop in velocity and density. The horizon marks a major transition in the seismic facies from a mostly irregular reflection pattern to a predominantly parallel one. Layered sediment deposition at Site 909 (Myhre et al., 1995b) is accompanied by step like changes in kaolinite (upward increase) and the smectite/illite ratio (upward decrease, Figs. 6g, h) suggesting abrupt changes in the clay mineral provenance. The whole sediment succession between MB08 and the seafloor is characterized by closely spaced, parallel to sub-parallel, continuous reflectors. From these the highest amplitude reflectors were picked for the Molloy Basin seismic stratigraphy. In the topmost part between MB08 and MB07 there are several closely spaced reflectors with upward increasing amplitude from which MB07 is the strongest. The smectite/illite ratio is gradually increasing upward in this interval while kaolinite content and acoustic impedance show decreasing trends (Fig. 6). These changes occur within the middle of sedimentary unit IIIa for which extensive millimeter-scale lamination with compositional, grain-size and/or colour changes was observed

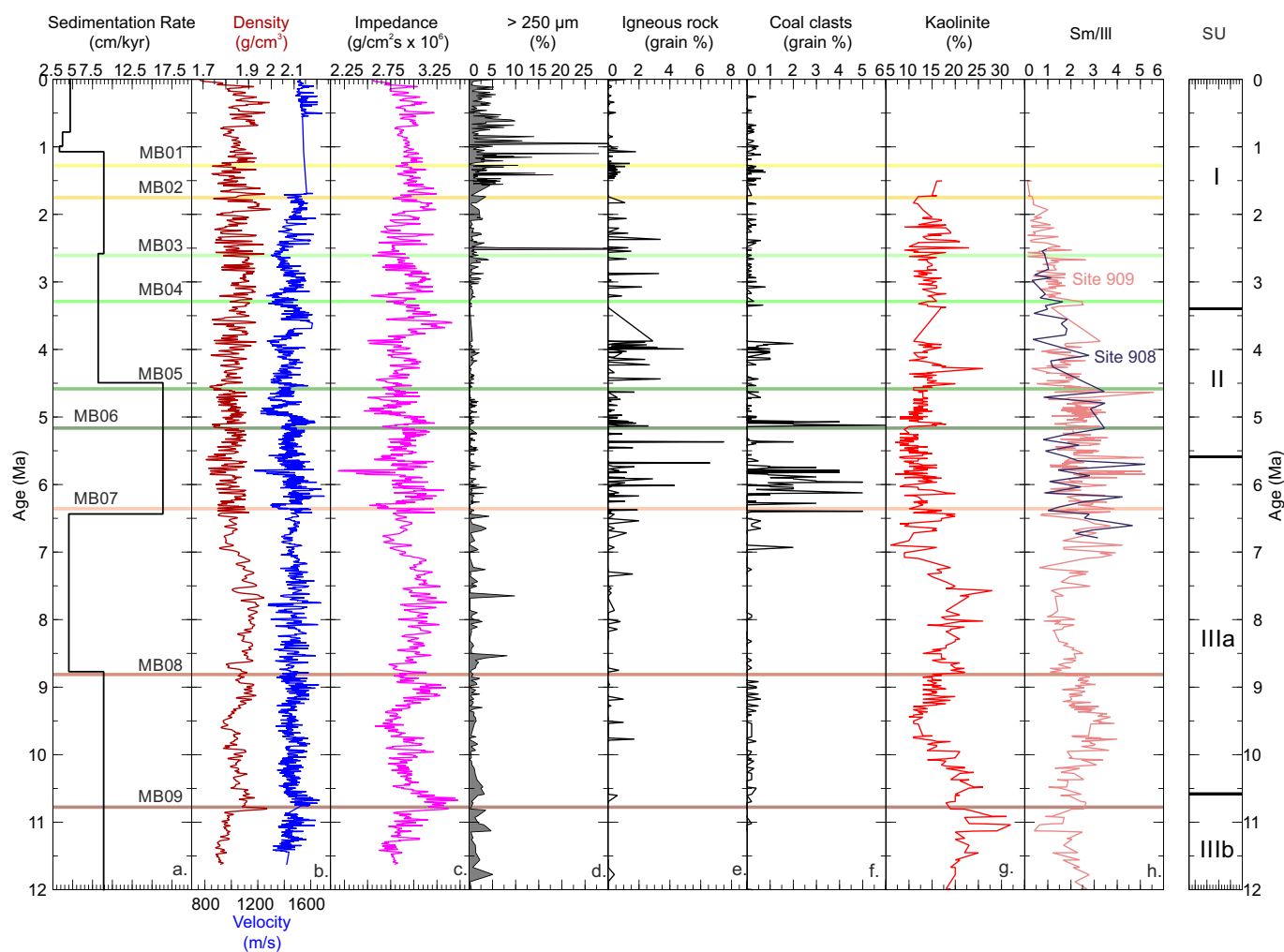


Fig. 6. Time series of sedimentation rates (a) and detrended physical properties (b-c) at ODP Site 909 in comparison to coarse-fraction (> 250 μm) grain size percentages (d) and results from coarse-fraction grain analysis given in percentage of the 125–500 μm fraction (Wolf-Welling et al., 1996): igneous rock particles (e) and coal clasts (f). Clay mineral records display %Kaolinite (g) and the smectite/illite ratio (h). In h the smectite/illite ratio for Sites 908 (Knies et al., 2014) is shown for comparison. SU = Sedimentary Unit. Coloured horizontal lines mark seismic reflectors.

(Myhre et al., 1995b).

Reflector MB07 at 4.13 s TWT corresponds to prominent step like changes (upward reductions) in velocity and impedance at c. 644 mbsf (Fig. 2), however no major lithological change is obvious from the core descriptions and photos at this depth. The dominant lithology in this interval is dark gray silty clay with occasionally minor (up to 10%) amounts of carbonate. The changes in physical properties at MB07 are accompanied by elevated smectite content (Fig. 6h).

The seismic facies between MB07 and MB06 is characterized by a series of parallel, moderate amplitude reflectors from which the strongest ones correspond roughly with the boundary between units IIIa and II. The sediment composition remains relatively uniform, and exhibits a range of structures from well-defined laminations to extremely mottled and burrowed colour bands (Myhre et al., 1995b). In Unit II beds of dark-coloured silty clays containing few fossils reflect the delivery of terrigenous material from suspension.

MB06 is another high amplitude reflector associated with rapid changes in velocity and density likely reflecting variations in fine sand accumulation (Fig. 7d). At this level (449 mbsf) prominent maxima in the percentages of kaolinite, coal clasts, and igneous rock fragments are observed (Fig. 6e–g).

Between reflectors MB06 and MB05 the internal parallel reflectors appear to be weaker in amplitude than below (Fig. 2g). In this interval of sedimentary unit II extensive laminae are composed of millimeter-scale compositional, grain-size and/or colour changes and reflect a record of variable, possibly rhythmic, depositional processes (Myhre et al., 1995b). Between CDPs 6500 and 7500 (Fig. 5a) the two reflectors bound another lens shaped sediment package with internal chaotic to transparent seismic reflection character.

The interval between MB05 and MB04 also shows a stratified seismic facies with relatively weak internal reflections (Fig. 2g). The recovered sediments are described as fairly homogenous in spite of variations in sand content (Myhre et al., 1995b). A few reflectors of moderate amplitude occurring in this uppermost sedimentary unit II seem to be related to increased sand content around 300 mbsf (Fig. 2a).

Reflector MB04 at 3.714 s TWT (c. 240 mbsf) represents the top of a band of three narrow reflectors (Fig. 2g) and roughly correlates with the boundary between the largely homogeneous sedimentary unit II and unit I. The latter one reveals contrasting textures, a range of colours and the presence of dropstones. The variations in physical properties causing the reflector band below MB04 are possibly due to the variable sand content at the base of Unit I (Fig. 2a), however this inference is speculative since sand content was not measured in the uppermost sedimentary unit II due to very low core recovery.

Reflectors MB03, MB02 and MB01 all occur within the uppermost 248.8 mbsf thick sedimentary Unit I (Fig. 2). In this unit a relatively fine-grained matrix consisting of colour-banded clays and clayey muds contains varying amounts of sand and dropstones (>1.0 cm diameter) representing ice-rafted detritus (IRD). Seismic reflections in this interval are numerous, closely spaced and of variable strength. Major reflector MB03 at 3.652 ms TWT (c. 184 mbsf) is caused by density peaks in an interval of enhanced IRD input (Figs. 2, 6b), while reflectors MB02 (108 mbsf) and MB01 (65 mbsf) both are caused by impedance reductions following peaks in IRD supply (Fig. 6c, d).

Sub-vertical faults are visible throughout the seismic section (Fig. 5a, tagged in supplementary Fig. 3) and appear to be separated into two depth levels (tiers). The deeper tier of these faults, possibly reflecting tectonic activity, lies below the termination of Site 909 and characterizes reflective sequences filling the basement troughs. The shallower tier, likely polygonal faults (e.g. Cartwright et al., 2003), extends from reflector MB08 upward. Westward from CDP 5450 these faults mostly terminate below MB04 while eastward they extend into increasingly younger strata but do not reach the sea floor.

5. Discussion

5.1. A new age model for ODP Site 909

In this chapter we revise the age model for Hole 909C (Winkler et al., 2002; Wolf-Welling et al., 1996) and use our new palynostratigraphic and published biostratigraphic data (Myhre et al., 1995b; Poulsen et al., 1996; Spiegler, 1996) to assign ages to intervals in the shipboard paleomagnetic measurements. All ages of polarity reversals are reported according to Ogg (2020).

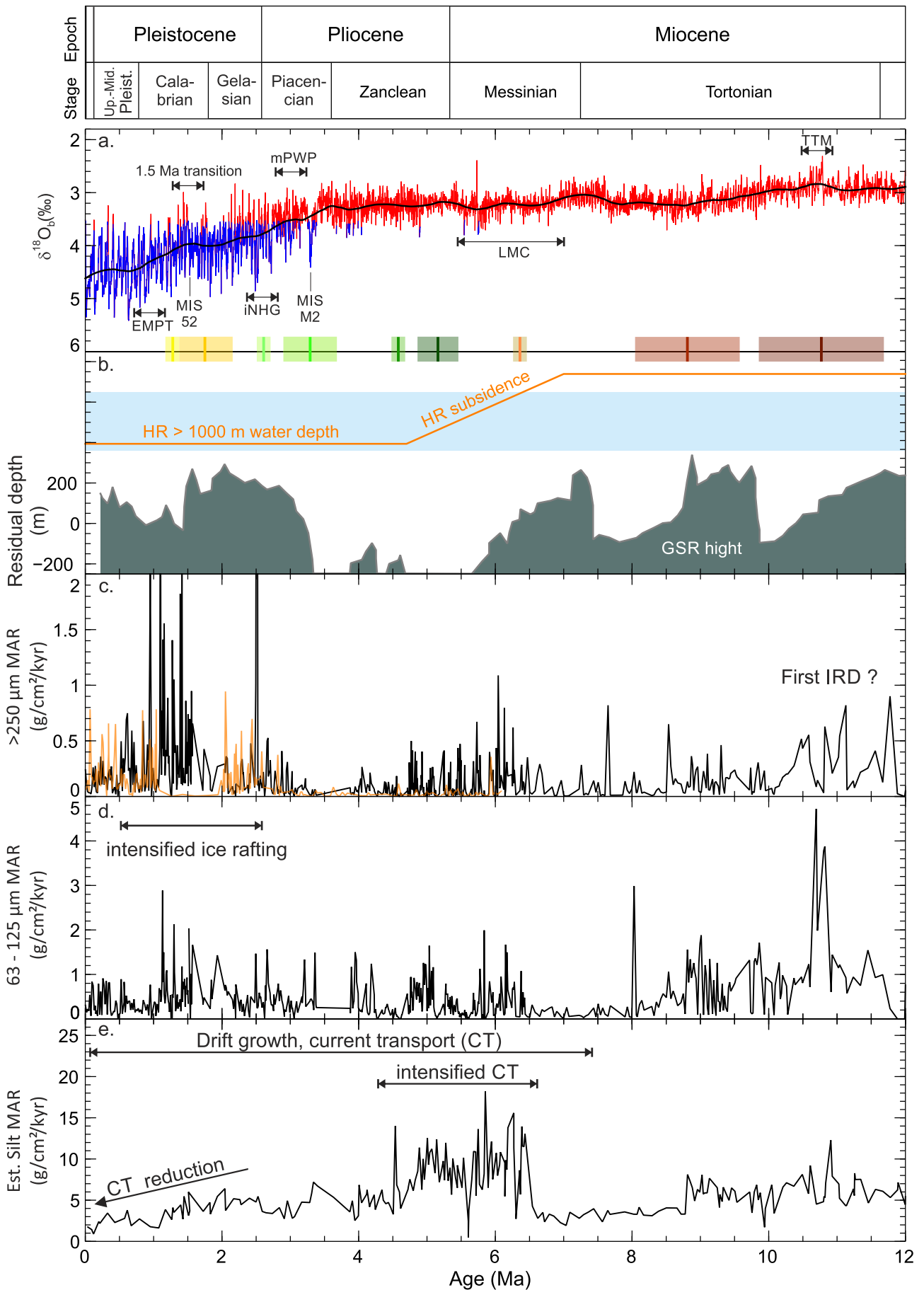
For the uppermost 90 mbsf inclination measurements vs. depth for Holes 909A and 909B (Myhre et al., 1995b) show a fair degree of correlation. The Brunhes Chron and the Jaramillo Subchron are definitely identified in both holes, indicating that identified magnetic transitions in this interval (Fig. 3, Table 1) are reliable.

For Hole 909C that was cored deeper than 85 mbsf, two interpretations of the inclination record were initially proposed (see supplementary Table 2), but biostratigraphic data only provided very basic age control for both models at that time (Myhre et al., 1995b). Age model 2 of Myhre et al. (1995b) has previously been preferred and in subsequent studies (Matthiessen et al., 2009b; Winkler et al., 2002; Wolf-Welling et al., 1996) was supplemented only by a single biostratigraphic age fix point of unknown origin (Fig. 4 and supplementary Table 2). Unfortunately, the interpretation of the inclination record is not discussed in any of these publications hampering a detailed comparison. Therefore, to achieve an unambiguous magnetostratigraphic interpretation below 90 mbsf, only clear magnetic reversals with palynological constraints from their immediate vicinity (Fig. 3) are used in our current study.

The HO of *Barssidinium graminosum* is likely a useful stratigraphic marker in the Atlantic sector of the high northern latitudes for the top of the Pliocene. It is almost synchronous in the North Atlantic region between 2.74 and 2.77 Ma (Aubry et al., 2020 and references therein), while in Hole 642A in the eastern Nordic Seas the HO is close to 3 Ma (De Schepper et al., 2017; De Schepper and Mangerud, 2018). The HO of *Barssidinium pliogenicum* is probably younger and has been observed in lower Pleistocene sediments (Aubry et al., 2020 and references therein). The identified HO of *Barssidinium* spp. (*B. graminosum*, *B. pliogenicum*) at 200.92 mbsf supports the identification of Chron C2An.1n within the upper part of the Matuyama Chron (Myhre et al., 1995b) and suggests that the inclination reversal at 181.75 mbsf marks the Gauss-Matuyama reversal (C2r.2r/C2An.1n) at 2.595 Ma (Fig. 3).

The HO of *Reticulatosphaera actinocoronata* is a robust supraregional bioevent in the North Atlantic region and is dated to the mid-Zanclean (Schreck et al., 2012). In Hole 642B from the Norwegian Sea, *R. actinocoronata* disappeared at the transition of Subchron C3n.2n to C3n.2r (4.64 ± 0.15 Ma) (De Schepper et al., 2017), while it disappeared in the upper part of Chron C3 (c. 4.5 Ma Schreck et al., 2012) in Hole 907A from the Iceland Sea. Therefore, the reversal in inclination from normal to reverse at 338.85 mbsf in Hole 909C, located only slightly above the HO of *R. actinocoronata* at 339.14 mbsf, is attributed to the top of Subchron C3n.2n (4.493 Ma, Fig. 3). In contrast, model 2 of the shipboard interpretation as used by Wolf-Welling et al. (1996) and Winkler et al. (2002) assigned this polarity change to the top of the slightly older Subchron C3n.4n (4.977 Ma).

Both the HO and HCO of the marine acritarch *Decahedrella martinheadii* are useful for identifying Messinian sediments in the Nordic Seas and Arctic Ocean but the HCO is a more robust bioevent than the HO (Matthiessen et al., 2009a; Schreck et al., 2012). The HCO is recorded at the top of Subchron C3An.2n in Hole 907A and dated to 6.5 Ma (Schreck et al., 2012). This bioevent at 657.22 mbsf occurs in an interval with normal polarity in Hole 909C and consequently, the reversal in inclination at 657 mbsf (Fig. 3) is assigned to the top of the normal Subchron C3An.2n (6.386 Ma). This age is significantly younger (c. 2.4 Myr) as postulated by both shipboard paleomagnetic age models by Myhre et al. (1995b) who, having only limited biostratigraphic control information



(caption on next page)

Fig. 7. Age assignments of interpreted seismic reflectors (coloured vertical lines, estimated age uncertainty is indicated by shaded backgrounds) in the Molloy Basin in comparison to (a) benthic oxygen $\delta^{18}\text{O}$ isotope compilation over the last 12 Ma (Westerhold et al., 2020), (b) schematic summary of Hovgaard Ridge subsidence (Knies et al., 2014) and Greenland-Scotland Ridge residual depth variability which is negatively correlated with the percentage of Northern Component Water (NCW) (Poore et al., 2006), (c. - e.) accumulation rates of coarse grained (>250 μm) sand (Wolf-Welling et al., 1996), fine grained (63–125 μm) sand (Wolf-Welling et al., 1996), and silt classified in smear slide analyses (Myhre et al., 1995b). Abbreviations: (a.) EMPT = Early Middle Pleistocene Transition, mPWP = mid-Piacenzian Warm Period, iNHG = intensification of Northern Hemisphere Glaciation, MIS = Marine Isotope Stage, TTM = Tortonian Thermal Maximum, (b.) HR = Hovgaard Ridge, GSR = Greenland Scotland Ridge, (c.) IRD = Ice Rafted Detritus.

available, associated the reversal with the top of Chron C4An.

The HO of *Labyrinthodinium truncatum* is a marker for upper Tortonian sediments in the North Atlantic region (Schreck et al., 2012). The HO is well-defined in Hole 907A and its age of 8.4 Ma was found to be older by c.1 Myr than at most sites in the northeast Atlantic region (Schreck et al., 2012). Therefore, we infer that the clear reversal in inclination at 762.40 mbsf (Fig. 3) below the HO at 760.185 mbsf must be older than 8.4 Ma and corresponds to the C4r.2r/C4An boundary at 8.771 Ma. Previously, both shipboard age models assigned this stratigraphic level to the C4Ar.3r/ C5n.1n boundary (9.786 Ma) (Myhre et al., 1995b), probably because the upper part of Chron C5 is characterized by a long interval with normal polarity (Fig. 3).

The chronostratigraphy of the lower part of Hole 909C, in particular Unit IIIb, is difficult to assess because of the absence of robust bioevents. Poulsen et al. (1996) noted that samples below 1020 mbsf comprise few species lacking any biostratigraphic marker which is supported by our new observations. The palynological restudy of Hole 909C could not confirm the HOs of *Aptodinium australiense*, *A. spirioides*, and *Distatodinium paradoxum* that are critical species in the initial biostratigraphy of Poulsen et al. (1996). This may be explained by the low and isolated occurrences of the stratigraphic marker species that might have been caused by reworking. Nonetheless, these species disappear in the Langhian to Serravallian (Anthonissen, 2012).

Although we hesitate to use lowest occurrences of palynomorphs as stratigraphic datums, these place some constraints on the age of the base of Hole 909C. The LO of *Decahedrella martinheadii* at 914.08 mbsf might be potentially useful to define the base of the Tortonian (Schreck et al., 2012). Schreck et al. (2012) give an age of 10.5 Ma for the LO.

The LO of *Labyrinthodinium truncatum* was used to date sediments above 98R-CC (1020.0 mbsf) to the Langhian (Poulsen et al., 1996) but recent studies indicate a LO in the North Atlantic region in the uppermost Burdigalian (Louwey and De Schepper, 2010; Sangiorgi et al., 2021; Soliman et al., 2012 and references therein). In this study *L. truncatum* has been observed below the LO of Poulsen et al. (1996) at the base of the hole (1062.2 mbsf) indicating that the base is younger than uppermost Burdigalian. This is not in conflict with a Langhian age at 1011 mbsf (Poulsen et al., 1996).

The LO of *Operculodinium? eirikianum* might be additionally useful to constrain the age of the base (1062.2 mbsf) of Hole 909C, but it is not well calibrated in the Atlantic sector of the high northern latitudes (Schreck et al., 2012). Schreck et al. (2012) observed the LO in Hole 907A from the Iceland Sea at the base of Subchron C5Ar in the early Serravallian at 13.0 Ma. In northern Italy *O.? eirikianum* appeared at the top of Subchron C5ABr at c. 13.6 Ma (Zevenboom, 1995). In the northeast Atlantic IODP Site 1318, the LO has moved from within Subchron C5ACn (c. 14 Ma; Louwey et al., 2007) to within Subchron C5ADn (c. 14.3 Ma; Quaijtaal et al., 2018) and recently to the Burdigalian/Langhian transition (Sangiorgi et al., 2021). Therefore, similar to *L. truncatum*, the occurrence of *Operculodinium? eirikianum* constrains the age for the base of Hole 909C to younger than uppermost Burdigalian.

Calcareous microfossils rather constrict the basal age to the Serravallian (Myhre et al., 1995b; Spiegler, 1996). The occurrence of *Globigerina bulloides* in Samples 70R-5, 89–93 (756.49 mbsf) and 76R-1, 96–98 (808.56 mbsf), was interpreted to indicate the upper Miocene and the base of the upper Miocene was set between 809 and 819 mbsf (Spiegler, 1996). However, *G. bulloides* is also present close to the base of Hole 909C in Sample 103R-2, 3–7 at 1059.53 mbsf where it co-occurs

with *Globorotalia scitula*. Anthonissen (2012) compiled stratigraphic information from a number of DSDP and ODP sites in the northern North Atlantic and Nordic Seas and gives an age of 14.7 Ma for the LO of *G. bulloides*. *Globorotalia scitula* appeared also in sediments younger than base middle Miocene (planktonic foraminifer zone N9; Spiegler, 1996) but Anthonissen (2012) arrived at a younger LO in the northern North Atlantic and Nordic Seas at the base of the Serravallian (13.8 Ma).

The occurrence of calcareous nannofossils *Helicosphaera carteri*, *Coccolithus miopelagicus* and *Cylicargolithus abisectus* in Sample 909C-101R-2, 26 cm (1050.16 mbsf) to Sample 909C-102R-CC (ca. 1058 mbsf) below a coccolith-free interval was interpreted to indicate an earliest Miocene age while Paleogene coccoliths such as *Dictyococites bisectus* may suggest a latest Oligocene age (Myhre et al., 1995b). If these species were considered reworked, the early Miocene marker species may also be indicative for younger sediments. Wei (1998) recorded these three species in Hole 918D from the southeast Greenland margin with HOs of *C. abisectus* and *C. miopelagicus* in Serravallian sediments according to strontium isotope stratigraphy (Israelson and Spezzaferri, 1998) which supports the interpretation based on planktonic foraminifera stratigraphy.

We conclude that both the calcareous microfossil and palynomorph stratigraphy suggest a younger age for the base of Hole 909C than previously published by Wolf-Welling et al. (1996) and Winkler et al. (2002) (Fig. 4). The available biostratigraphic information does not support their only biostratigraphic datum at the base of Hole 909C. An exact age is difficult to assign to the oldest cored sediments but these are certainly younger than the Serravallian/Langhian boundary at 13.82 Ma (Fig. 3). A definite stratigraphic interpretation is further hampered by possible stratigraphic breaks in section 909C-89-R (940 mbsf) and at the base of section 909C-87-R (923.40 mbsf) suggested by conspicuous reworking of palynomorphs (Poulsen et al., 1996). Moreover, an uppermost middle to late Miocene age (c. 11.6 Ma) for the base of Hole 909C cannot be ruled out because meter-scale slump structures below 923.4 mbsf indicate mass-transport deposits (Myhre et al., 1995b) and therefore an increased possibility for rapid sediment accumulation and reworking of the palynomorph assemblages.

In the following the new age model is used to discuss significant changes in climate, oceanography and tectonics that are nowadays associated with major seismic reflectors.

5.2. Interpretation of deep seismic reflectors and the onset of IRD deposition

Compilations of oceanic crustal ages based on magnetic anomaly identifications suggest an age between c. 14.5 Ma (Seton et al., 2020) and c. 15.3 Ma (Straume et al., 2019) for the crust below Site 909. According to Müller et al. (2008), the age uncertainty of such crustal age calculations for the Fram Strait may be up to several million years. In line AWI-20020300 acoustic basement is not unambiguously identifiable below Site 909 (Fig. 5a).

The reflectors at 4.638 s (c. 1228 mbsf) do not represent the top of the oceanic crust as previously inferred (Myhre et al., 1995b), but rather layered deposits on top of a rifted/rotated crustal block. By extrapolating the sedimentation rates from the deepest dated section, the top of the reflector series at c. 1228 mbsf has an age of 14.7 ± 1.3 Ma. Without groundtruthing by drilling we can here only speculate about the origin of the layered deposits. They may be related to older lithified sediments filling the basement troughs (Ritzmann et al., 2004) or to lava flows

from the paleo Knipovitch-/Svyogator Ridge spreading center. Since Site 909 encountered high gas concentrations in the lowermost section (Myhre et al., 1995b) and a long-lived gas hydrate- and free gas-charged drift system at the Svyatogor Ridge has been identified (Johnson et al., 2015), the deep strong reflectors may also be an indication for the presence of free gas.

The lowermost reflector correlated with Site 909 is MB09 at 4.410 s (c. 941 mbsf). This reflector is dated to c. 10.8 Ma and correlates with increased deposition of coarse-grained material (Fig. 6d) and enrichment of kaolinite in the fine fraction (Fig. 6g). Knies and Gaina (2008) interpreted these concurrent peaks of kaolinite and coarse-grained material as indicators for iceberg transport of glacially eroded materials from the uplifted northern Barents Sea towards the Fram Strait. According to their age model in use (Winkler et al., 2002), this modern-like ice rafting pattern established already c. 15–14 Ma ago. However, this timing strongly relies on biostratigraphic age picks from sedimentary Unit IIIb comprising the depth interval from 923.4 to 1061.80 mbsf (base of Hole 909C). This unit is characterized by discontinuous and inclined internal seismic reflections, very low recovery (Fig. 2), and the occurrence of slump structures (Myhre et al., 1995b) suggesting that reworking of microfossils was severe below 923.4 mbsf. Our new stratigraphy suggests a much younger (<13.8 Ma, Table 1) age for the base of Hole 909C and subsequently, the kaolinite and IRD enrichments around 940 mbsf associated with reflector MB09 have a Tortonian (c. 10.8 Ma) age (Table 2) and are thus c. 3–4 Ma younger as previously inferred. Furthermore, these peaks postdate, instead of predate (Thiede et al., 1998), earliest ice rafting at the Vøring Plateau c. 12.6 Ma, Fronval and Jansen (1996) and occur well after the cooling of the Middle Miocene Climate Transition (MMCT, (c. 15–13 Ma, Holbourn et al., 2013). Possible earlier (>10.8 Ma) ice rafting in the Fram Strait cannot be excluded here since angular and sub-rounded coarse fraction material was found down to the base of Site 909 (Wolf-Welling et al., 1996) and may also be present below the termination of the drillsite. However, this lowermost coarse material stems from disturbed intervals with stratigraphic breaks (see 4.2) which suggests that local redeposition may have occurred.

The new 10.8 ± 0.9 Ma age assignment for the Fram Strait pulse of coarse fraction detritus (MB09) corresponds to evidence for ice rafting from SE Greenland at c. 11 Ma (Helland and Holmes, 1997) and to the first occurrence of dropstones on the eastern Iceland Plateau (c. 10.7–10.2 Ma, Schreck et al., 2013). Age wise MB09 also could be correlated with a regional intra-Miocene seismic unconformity at the NE Greenland margin (Døssing et al., 2016) and with a strong reflector in the Nansen Basin (Table 3) that was interpreted to reflect a major palaeoceanographic event related to the opening of the Fram Strait (Engen et al., 2009). Interestingly c.10.8–10.7 Ma is also the time of the Tortonian Thermal Maximum (Westerhold et al., 2020), a remarkable warming episode (Fig. 7a) associated with a massive negative carbon isotope shift (Holbourn et al., 2013) and a rapid sea level change of ± 50 m (Miller et al., 2020).

5.3. Onset of current controlled sedimentation during the Tortonian

From reflector MB08 (c. 8.8 Ma) upward seismic layering in the basin is more and more pronounced and parallel (Figs. 2g and 5a). The lowermost of these parallel reflectors overlap the structural highs and may thus be regarded as hemipelagites deposited in a relatively restricted basin (Myhre et al., 1995b). In the uppermost interval between MB08-MB07 reflector geometry indicates aggradational deposition with asymmetric build-ups over highs (Fig. 5). This geometry, the gradual change in clay mineral composition starting at c. 7.5 Ma (Fig. 6), and the sediments being composed of up to 50% silt (Myhre et al., 1995b) suggest an increasing influence of the ocean current system from the late Tortonian (<7.5 Ma) onward. From the seismically layered, aggradational structure and the low relief, we conclude that the whole sediment package above this level may be classified as a sheeted drift. This drift

type is indicative for a mostly low energetic tabular current regime that is regionally stable (e.g. Rebesco et al., 2014a). In the earliest phase of drift formation sedimentation rates were at moderate values of 4.5 cm/kyr (Fig. 6a) but later on strongly increased (see 5.4). The sediment drift in the central Fram Strait is accompanied by other, mostly younger contouritic features, like mounded drift structures and sediment waves, that were documented for the eastern vicinity of the Molloy Basin (Gebhardt et al., 2014) and elsewhere along the main flow of the WSC (Mattingsdal et al., 2014; Rebesco et al., 2013; Rydningen et al., 2020).

Today, ocean circulation in the Molloy Basin is largely governed by a western, recirculating branch of the WSC (Beszczynska-Möller et al., 2012) which is turning in the area around the Molloy Deep (Fig. 1a). Compared to the northbound WSC branch on the eastern side of the Fram Strait, this return flow is relatively sluggish (Fig. 1c). Our interpretation suggests that this scenario may have been first established c. 7–8 Ma ago which is significantly later as the inferred middle Miocene start of contouritic deposition (base of YP-2 Unit) at the Yermak Plateau (Geissler et al., 2011; Mattingsdal et al., 2014). Geissler et al. (2011) roughly correlated the base of YP-2 to the base of stratigraphic unit IIIa at ODP Site 909 and assigned an age of c. 14.8 Ma according to (Knies and Mann, 2002). According to our new stratigraphy the base of unit IIIa is now at c. 10.8 Ma (Fig. 7) which is in better agreement with Mattingsdal et al. (2014) who derived c. 11 Ma for the onset of current deposition at the Yermak Plateau. Even if we acknowledge a large (1–2 Myr) uncertainty for the c. 11 Ma age at the Yermak Plateau it seems likely that current controlled sedimentation on the northern Svalbard margin started earlier than in the Molloy Basin. This would imply that for some time between the middle and late Miocene the WSC consisted only of the northbound branch. This could be due to a narrower bottom water passage and a restriction of the Molloy Basin by a very shallow (likely subaerial) Hovgaard Ridge (Engen et al., 2008). The onset of the recirculating branch at c. 7.5 Ma could have been triggered by stronger NAC inflow (Poore et al., 2006) caused by a subsidence episode of the Greenland-Scotland Ridge crest (Wright and Miller, 1996) (Fig. 7b). A strengthening of AMOC at the same time (Lear et al., 2003) was related to a major step in the closure of the Central American Seaway (Kirillova et al., 2019). This occurred when the AAG was wider (Engen et al., 2008; Straume et al., 2020) but the crest of the Hovgaard Ridge still subaerially exposed or in very shallow water.

5.4. Enhanced sediment transport during the latest Miocene to early Pliocene

Reflector MB07 at 4.13 s TWT (c. 644 mbsf) which corresponds to prominent seismic horizons identified at the Yermak Plateau and in the Nansen Basin (Geissler and Jokat, 2004) (Table 3) marks a change in the sedimentary regime of the central Fram Strait at c. 6.4 Ma (Table 2). At this time a significant (5 cm/kyr to 16 cm/kyr) increase in sedimentation rates occurred (Fig. 6a) and these high rates, accompanied by high smectite content (Fig. 6h), prevailed until c. 4.6 Ma (MB05). Knies et al. (2014) proposed that at least during the early Pliocene the smectite-rich sediments (high Sm/I ratio) might have been an alteration product from volcanic sources, which is supported by higher amounts of igneous material in the coarse-grained sediment above MB07 (Fig. 6e).

Although, the overall percentage of coarse-grained sediment is generally low in the interval between MB07 and MB05 (Figs. 2a and 6d), the MAR records of IRD (63–125 μm , >250 μm) show local maxima (Fig. 7c, d). This suggests that moderate ice rafting occurred from c. 6.4 to 4.6 Ma in the Molloy Basin, although the signal is diluted by the much higher deposition of current transported clay and silt sized material. The ice rafting falls within the late Miocene cooling phase (Steinthsordottir et al., 2021) between c. 7 and 5.5 Ma (Fig. 7a). During this time interval sea surface temperatures in high latitudes of both hemispheres cooled by up to 8 °C and the pole-to-equator temperature gradient increased (Herbert et al., 2016). Thus, in addition to evidence from the east Greenland margin (Bierman et al., 2016; Pérez et al., 2018) the increase

Table 3
Comparison of seismic stratigraphies in the Fram strait area covering the last 12 Ma.

Study	Area	Reflectors or seismic unit boundaries (age in Ma)								
This Study	MB ¹	MB01 (1.3)	MB02 (1.8)	MB03 (2.6)	MB04 (3.3)	MB05 (4.6)	MB06 (5.2)	MB07 (6.4)	MB08 (8.8)	MB09 (10.8)
Eiken and Hinz (1993)	MB ¹			GS3/GS4 (u. Plioc.)		GS2/GS3 (Pliocene)	GS1/ GS2 (l. Plioc.)			
Eiken and Hinz (1993)	BB ²	BB3/BB4 (Pleistocene)			BB2/ BB3 (u. Plio.)			BB1/ BB2 (u. Mioc.)		
Berger and Jokat (2009)	GB ³ , MB ¹ , BB ²			NA-1/ NA-2 (3.0)		NA2/NA3 (5.0)		NA3/ NA4 (14.0)		
Døssing et al. (2016)										IMU (10–15)
Geissler and Jokat (2004)	YP ⁴			YP2/YP3 (2.6)				YP1/ YP2 (6–7)		
Mattingsdal et al. (2014)	YP ⁴	Blue (1.5)		Green (2.5)			Purple (5.2)			
Butt et al. (2002)	s-w BS ⁵	R5 (1.4)	R6 (1.6)	R7 (2.3)						
Harishidayat et al. (2021)	s-w BS ⁵	H5 (1.5)		H9 (2.7)			H10 (5.3)			
Faleide et al. (1996), Fiedler and Faleide, (1996), Solheim et al. (1996)	n-w BS ⁶	R5 (1.0)		R7 (2.3)						
Rebesco et al., (2014a)	n-w BS ⁶	R4A (1.3)	R6 (2.1)							
Alexandropoulou et al. (2021)	s-w BS ⁵ n-w BS ⁶	R4A (1.2)	R6 (1.8)							
Geissler and Jokat (2004)	n BS ⁷ NB ⁸			NB2/ NB3 (2.6)				NB1/ NB2 (6–7)		
Engen et al. (2009)	n BS ⁷ NB ⁸	NB4a/NB4b (1.5)		NB3/ NB4a (2.6)						NB2/ NB3 (10.0)
Lasabuda et al. (2018)	n BS ⁷ NB ⁸	NB3a/NB3b (1.5)		NB2/ NB3a (2.7)						

¹ Molloy Basin.

² Boreas Basin.

³ Greenland Basin.

⁴ Yermak Plateau.

⁵ south-western Barents Sea.

⁶ north-western Barents Sea.

⁷ northern Barents Sea.

⁸ Nansen Basin.

in IRD accumulation at Site 909 provides further indications for late Miocene transient glaciations in the Northern Hemisphere.

Apart from the moderate IRD deposition we interpret the stratified seismic signature (Fig. 2g), the laminated sedimentary structures, and the high sedimentation rates between c. 6.4 and 4.6 Ma (Fig. 4) as indicative of enhanced sediment transport into the Molloy Basin by the western recirculating branch of the WSC. For the same time period, a marked increase in sedimentation rates is also reported for the central Yermak Plateau (ODP Site 910) where migration of a buried detached contourite drift indicates enhanced current activity of the eastern branch of the WSC (Mattingsdal et al., 2014). The changing sedimentation rates in the Molloy Basin are likely related to the subsidence history of the Hovgaard Ridge (Fig. 7b). A distinct unconformity at ODP Site 908 (Myhre et al., 1995a) indicates that the ridge was in very shallow water or even sub-aerially exposed from c. 25 Ma (Eldrett et al., 2019) to c. 6.7 Ma (Matthiessen et al., 2009a). The following time interval (c. 6.7 to 4.7 Ma) for which a continuous subsidence of the Hovgaard Ridge and a widening/deepening of the central Fram Strait is postulated (Knies et al., 2014) exhibits the highest sedimentation rate in the Molloy Basin (Fig. 6a). With the new stratigraphy grain size and clay mineralogy

records from ODP Sites 908 and 909 are better synchronized (Figs. 6h and 7c). We argue that igneous grains, coal fragments and smectite-rich fines enriched in the high-sedimentation rate interval at Site 909 (Fig. 6) were either directly derived from the subsiding Hovgaard Ridge and/or were eroded and current entrained from volcanic provinces along the western Barents Shelf margin (Senger et al., 2014 and references therein). This margin underwent a Miocene/Pliocene uplift phase (e.g. Green and Duddy, 2010) which is thought to have preconditioned the landscape to host perennial dynamic ice fields (Knies et al., 2014) that caused elevated erosion rates. Thus both enhanced sediment supply and a changing current pattern due to the ongoing opening of the AAG likely caused the elevated sedimentation rates at Site 909. The change in sedimentation rate occurs in a time interval for which an increase of North Atlantic Deep Water (NADW) production (Poore et al., 2006) and a strengthening of AMOC (Karas et al., 2017) is inferred which likely led to a stronger NAC/WSC flow at that time.

Within the high sedimentation rate interval, high amplitude reflector MB06 occurs at 5.2 ± 0.3 Ma and reflects variations in fine sand accumulation during the Messinian (Fig. 7d). The horizon correlates in time/age with the north-eastward change in sediment drift depocentres in the

Davis Strait (Nielsen et al., 2011) and with recently reported reflector H10 at the south-western Barents Sea margin (Harishidayat et al., 2021) (Table 3). There the upper slope became dominated by channels with associated sediment lobes and mass transport deposits in the earliest Pliocene (c. 5.3 Ma). In the Molloy Basin MB06 and MB05 bound a lens shaped sediment package with internal chaotic to transparent seismic reflection character at CDPs 6500–7500 in line AWI-20020300 (Fig. 5a, supplementary Fig. 3). These features are interpreted to reflect local lateral sediment mass transport between c. 5.2 and 4.6 Ma (e.g. Posamentier and Martinsen, 2011).

After c. 4.6 Ma (Reflector MB05) sedimentation rates in the Molloy Basin dropped to 8 cm/kyr (Fig. 6a). At this time the Bering Strait circulation reversed from a southward flow to a northward flow (Verhoeven et al., 2011) which led to a reorganization of Nordic Seas surface circulation including the development of a modern-like EGC (De Schepper et al., 2015). Consequently import of fresher, cooler Arctic Water and a major expansion of the sea ice cover east off Greenland were initiated (Clotten et al., 2019). No significant reductions in NADW/AMOC/NAC are reported for that time, thus we speculate that the lowered sediment transport to Site 909 is due to a reduction in suspension load of the WSC related to further subsidence of the Hovgaard Ridge and/or a redeposition of particles further southward by the EGC.

5.5. Major steps in Plio-Pleistocene Northern Hemisphere glaciation history

The uppermost seismic marker reflectors in the Molloy Basin are related to major steps in the intensification of Northern Hemisphere glaciation. The inferred age of c. 3.3 Ma for horizon MB04 suggests that the reflector band associated with MB04 (Fig. 2g) is related to the prominent glacial marine isotope stage (MIS) M2 which is an isolated cold stage punctuating the benthic oxygen isotope ($\delta^{18}\text{O}$) stratigraphy of the Piacenzian (late Pliocene) (Fig. 7a). The prominent (c. 0.65‰) $\delta^{18}\text{O}$ increase that defines MIS M2 predates the mid-Piacenzian Warm Period and has been seen as a premature attempt of the climate system to establish an ice-age world (De Schepper et al., 2013). At the Yermak Plateau this event is characterized by high abundance of IRD and maxima in kaolinite and illite interpreted to reflect erosion of kaolin-rich Mesozoic sediments during ice sheet advances in the northern, sub-aerially exposed Barents Sea (Knies et al., 2009). However, this glacially eroded material did not reach the central Fram Strait since at Site 909 IRD is largely diminished and the kaolinite record shows low amplitudes (Fig. 6g). The Site 909 sedimentary record rather indicates deposition under hemipelagic conditions with little or no glacial influence from Svalbard. Nevertheless, increased glacial weathering is also evident for Molloy Basin sediments as indicated by the replacement of smectite by chlorite and illite (Winkler et al., 2002) and a local maximum in fine sand particles (Fig. 2a). There is evidence from sea surface temperature and salinity proxies for weakening of the NAC/AMOC system that preceded MIS M2 by up to 300 kyrs (De Schepper et al., 2009; Karas et al., 2020). It is proposed that this weakening caused a reduction in northward heat transport and prepared the conditions for later ice growth on Greenland as documented by Kleiven et al. (2002).

Reflector MB03 has an inferred age of c. 2.6 Ma and therefore likely reflects the intensification of Northern Hemisphere glaciation (iNHG). This irreversible climatic deterioration that occurred around 2.7 Ma (Bartoli et al., 2005) has been found to manifest in global ice volume increase and synchronous ice sheet development on Greenland, Barents Sea, Scandinavia, and North America (Kleiven et al., 2002; Knies et al., 2009). In the AAG pulses of IRD occur between 2.7 and 2.4 Ma (Fig. 6d) and thus contemporaneous to a distinct supply of IRD-rich sediments on the Yermak Plateau and along the western Svalbard–Barents Sea margin between (Knies et al., 2009). The iNHG is also marked by prominent seismic reflectors across the southwestern Barents Sea margin (e.g. Fiedler and Faleide, 1996; Harishidayat et al., 2021; Laberg et al., 2012), the western Svalbard continental shelf (Solheim et al., 1996), the

northern Barents Sea (Engen et al., 2009; Faleide et al., 1996; Geissler and Jokat, 2004; Lasabuda et al., 2018), and the Yermak Plateau (Geissler and Jokat, 2004; Mattingsdal et al., 2014) which correlate with MB03 (Table 3). These seismic expressions of the iNHG have also been traced in mounded sediment drifts located along the western Yermak Plateau flank (Gebhardt et al., 2014), on the Vestnesa Ridge (Hustoft et al., 2009) and on the Svyatogor Ridge (Johnson et al., 2015). In all of these settings shifts towards higher sedimentation rates were associated with the iNHG. In the Molloy Basin sedimentation rates at the iNHG show only a slight increase (Fig. 6a) but the event is marked by enhanced transport of coarse-grained (sand sized) sediments by icebergs and sea ice (Fig. 7c, d). Also, the accumulation of silt likely sourced by (glacio-) fluvial input along the pathway of the WSC (Butt et al., 2000; Gebhardt et al., 2014) commenced (Fig. 7e). Both, drift growth in the Molloy Basin and significant changes in the migration of contouritic features elsewhere in the Fram Strait (Gebhardt et al., 2014) are indicators for a vigorous WSC/NAC/AMOC system after the iNHG rather than for a weak circulation (Poore et al., 2006). This conclusion is in agreement with results from modeling (Lunt et al., 2008) and environmental magnetic proxy indications for high Iceland–Scotland Overflow Water activity (Hayashi et al., 2020), both supporting the notion that Northern Hemisphere glaciation was amplified by the intensified AMOC after the closure of the Central American Seaway.

Reflectors MB02 (c. 1.8 Ma) and MB01 (c. 1.3 Ma) both can be related to a further increase in the intensity of Northern Hemisphere glacial–interglacial cycles that occurred around 1.5 Ma, the “1.5 Ma transition” around MIS 52 (Hodell and Channell, 2016). The enhanced IRD supply in the Molloy Basin (Fig. 7c) occurs synchronously with the occurrence of massive debris flows and IRD along the western Svalbard margin (Butt et al., 2000; Mattingsdal et al., 2014; Rebesco et al., 2014b; Solheim et al., 1998), while for the western Barents Sea ice-stream activity above the regional seismic reflector R5 (c. 1.5 Ma) is indicated by megascale lineations (Andreassen et al., 2004). A reduction in overflow of deep waters from the Nordic Seas into the North Atlantic at 1.6–1.3 Ma is inferred from Nd isotope (Khélifi and Frank, 2014) and benthic $\delta^{13}\text{C}$ (Hodell and Venz-Curtis, 2006). However, a possible related reduction in WSC intensity is not reflected in the sedimentation rates or accumulation rates in the silt grain size fraction (Figs. 6a, 7e) at Site 909 which stay at a constant level. A rather active WSC can also be inferred from the initiation of the Isfjorden and the Bellsund sediment drifts (Rebesco et al., 2013) in correspondence with suspended sediments becoming available during the development of trough mouth fans at the north-western Barents Sea margin at c. 1.2–1.3 Ma (Alexandropoulou et al., 2021; Rebesco et al., 2014b) (reflector R4A, Table 3). It should be noted that neither our age model nor the ones used by Rebesco et al. (2014b) and Alexandropoulou et al. (2021) have the resolution to resolve possible short term changes in sedimentation rates at c. 1.3 Ma.

A major decrease in the mass accumulation of all grain size classes (Fig. 7) occurs just above MB01 at c. 1 Ma, a time after which large-scale glaciations with repeated advances to the shelf edge in the Barents Sea have been inferred (Knies et al., 2009). The timing correlates with a significant prolongation and intensification of glacial–interglacial climate cycles (Fig. 7a) (Elderfield et al., 2012), the Early Middle Pleistocene Transition (Maslin and Brierley, 2015). This transition is associated with a perturbation of mean ocean carbon chemistry around 0.9 Ma and the beginning of weaker NADW export to the Southern Ocean (Venz and Hodell, 2002; Pena and Goldstein, 2014). Recently, it was hypothesized that Arctic-wide occurrence of thick shelf-ice in peak glacials could have blocked the Greenland–Scotland Ridge overflow, causing freshening of the entire Arctic Basin and the Nordic Seas (Geibert et al., 2021). The general low accumulation rate of grains $<63\ \mu\text{m}$ (Fig. 7e) in the Molloy Basin during the last 1 Myr may be related to this weakening of the AMOC system during extreme glacials. Also the accumulation of coarser grain sizes (Fig. 7c, d) was at a lower level in this interval indicating that deposition of IRD in the Fram Strait during these ice-dammed periods was also diminished. This may also be

attributed to a decrease in erosion capacity of the Kara–Barents Sea–Svalbard Ice Sheet since c. 0.78 Ma (Hjelstuen and Sejrup, 2021). The reduced erosion capacity could be a consequence of the subsidence of the Barents Sea below current sea level (Zieba et al., 2017) and the development of a fully marine ice sheet.

6. Conclusions

We derived a new high-resolution seismic stratigraphy of the last c. 12 Myr for the Molloy Basin (Fram Strait) that is based on an improved core-log-seismic integration and a revised age model for ODP Site 909. This age model is derived from newly identified biostratigraphic events that allow an improvement of the existing magnetic reversal chronology. The new seismic stratigraphy is used together with re-interpreted sedimentological data to infer changes in ice rafting and current transport in the AAG:

1. A coarse fraction pulse in the Fram Strait (reflector MB09) previously interpreted as evidence for ice rafting during the MMCT is newly dated at c. 10.8 Ma and thus occurred well after the climate deterioration of the MMCT during a time of low climate variability.
2. Current controlled sedimentation in the central Fram Strait started during the late Tortonian as indicated by the increasingly aggradational character of the layered deposits. A sheeted drift body began to form from sediments deposited by a western, recirculating branch of the WSC. The initiation of this contourite started later (c. 7.5 Ma) as the inferred formation of sediment drifts at the northern Svalbard margin (c. 11 Ma).
3. The time interval from c. 6.4 Ma to 4.6 Ma, bounded by reflectors MB07 and MB05, is characterized by profound changes in sediment supply and source. Strongly elevated sedimentation rates (> 16 cm/kyr) in this interval are interpreted to reflect enhanced current transport by a western branch of the WSC in conjunction with a higher suspension load possibly derived from the subsiding Hovgaard Ridge.
4. Late Pliocene to Pleistocene seismic marker horizons appear to be associated with IRD events and have assigned ages of c. 3.3 Ma (MIS M2), c. 2.7 Ma (iNHG), c. 1.8 Ma and c. 1.3 Ma (early Pleistocene transition). A significant reduction in accumulation rates after c. 1 Ma correlates with the Mid Pleistocene Transition towards longer and colder glacial periods that is accompanied by a weakening of the AMOC/NAC circulation.

In summary, we have shown that prominent changes in ice volume and oceanography during the last 12 Myr left marked imprints in the sedimentary cover of the Molloy Basin and that the presented new age model allows a better regional and global integration of proxy records from ODP Site 909. Together these findings may inspire further work on Site 909 material and support current planning activities for future drilling in the Arctic region.

Data availability

Presented data are available online at the Data Publisher for Earth and Environmental Science, PANGAEA (www.pangaea.de): <https://doi.org/10.1594/PANGAEA.943221>

Declaration of Competing Interest

The authors declare that they have no known competing financial interests or personal relationships that could have appeared to influence the work reported in this paper.

Acknowledgements

Funding was provided by the Deutsche Forschungsgemeinschaft

(DFG) under contract GEI 1783/6-1. Support by the Open Access Publication Funds of Alfred-Wegener-Institut Helmholtz- Zentrum für Polar- und Meeresforschung is acknowledged. The authors would like to thank Emerson E&P Software, Emerson Automation Solutions, for providing licenses for the seismic software Paradigm in the scope of the Emerson Academic Program. Constructive comments from three anonymous reviewers helped to improve the manuscript.

Appendix A. Supplementary data

Supplementary data to this article can be found online at <https://doi.org/10.1016/j.gloplacha.2022.103876>.

References

- Aagaard, K., Foldvik, A., Hillman, S.R., 1987. The West Spitsbergen current: disposition and water mass transformation. *J. Geophys. Res. Oceans* 92 (C4), 3778–3784. <https://doi.org/10.1029/JC092iC04p03778>.
- Alexandropoulou, N., et al., 2021. A continuous seismostratigraphic framework for the Western Svalbard-Barents Sea margin over the last 2.7 Ma: implications for the late Cenozoic Glacial history of the Svalbard-Barents Sea ice sheet. *Front. Earth Sci.* 9, 656732 <https://doi.org/10.3389/feart.2021.656732>.
- Andreassen, K., Nilsen, L.C., Rafaelsen, B., Kuilman, L., 2004. Three-dimensional seismic data from the Barents Sea margin reveal evidence of past ice streams and their dynamics. *Geology* 32 (8), 729–732. <https://doi.org/10.1130/G20497.1>.
- Anell, I., Thybo, H., Artemieva, I.M., 2009. Cenozoic uplift and subsidence in the North Atlantic region: Geological evidence revisited. *Tectonophysics* 474 (1), 78–105. <https://doi.org/10.1016/j.tecto.2009.04.006>.
- Anthonissen, E.D., 2012. A new Miocene biostratigraphy for the northeastern North Atlantic: an integrated foraminiferal, bolboformid, dinoflagellate and diatom zonation. *Newsl. Stratigr.* 45 (3), 281–307. <https://doi.org/10.1127/0078-0421/2012/0025>.
- Archie, G.E., 1942. The electrical resistivity log as an aid in determining some reservoir characteristics. *Trans. AIME* 146 (01), 54–62. <https://doi.org/10.2118/942054-G>.
- Aubry, A.M.R., De Schepper, S., de Vernal, A., 2020. Dinocyst and acritarch biostratigraphy of the late pliocene to early pleistocene at integrated ocean drilling program Site U1307 in the Labrador Sea. *J. Micropalaeontol.* 39 (1), 41–60. <https://doi.org/10.5194/jm-39-41-2020>.
- Bartoli, G., et al., 2005. Final closure of Panama and the onset of northern hemisphere glaciation. *Earth Planet. Sci. Lett.* 237 (1–2), 33–44. <https://doi.org/10.1016/j.epsl.2005.06.020>.
- Bassinot, F.C., 1993. Sonostratigraphy of tropical Indian Ocean giant piston cores: toward a rapid and high-resolution tool for tracking dissolution cycles in Pleistocene carbonate sediments. *Earth Planet. Sci. Lett.* 120 (3–4), 327–344. [https://doi.org/10.1016/0012-821X\(93\)90248-8](https://doi.org/10.1016/0012-821X(93)90248-8).
- Berger, D., Jokat, W., 2009. Sediment deposition in the northern basins of the North Atlantic and characteristic variations in shelf sedimentation along the East Greenland margin. *Mar. Pet. Geol.* 26 (8), 1321–1337. <https://doi.org/10.1016/j.marpetgeo.2009.04.005>.
- Beszczynska-Möller, A., Fahrbach, E., Schauer, U., Hansen, E., 2012. Variability in Atlantic water temperature and transport at the entrance to the Arctic Ocean, 1997–2010. *ICES J. Mar. Sci.* 69 (5), 852–863. <https://doi.org/10.1093/icesjms/fss056>.
- Bierman, P.R., Shakun, J.D., Corbett, L.B., Zimmerman, S.R., Rood, D.H., 2016. A persistent and dynamic East Greenland Ice Sheet over the past 7.5 million years. *Nature* 540 (7632), 256–260. <https://doi.org/10.1038/nature20147>.
- Breitzke, M., 2006. Physical properties of marine sediments. In: Schulz, H., Zabel, M. (Eds.), *Marine Geochemistry*. Springer, Berlin Heidelberg, pp. 27–71. https://doi.org/10.1007/3-540-32144-6_2.
- Briner, J.P., et al., 2020. Rate of mass loss from the Greenland Ice Sheet will exceed Holocene values this century. *Nature* 586 (7827), 70–74. <https://doi.org/10.1038/s41586-020-2742-6>.
- Butt, F.A., Elverhøi, A., Solheim, A., Forsberg, C.F., 2000. Deciphering Late Cenozoic development of the western Svalbard Margin from ODP Site 986 results. *Mar. Geol.* 169 (3), 373–390. [https://doi.org/10.1016/S0025-3227\(00\)00088-8](https://doi.org/10.1016/S0025-3227(00)00088-8).
- Butt, F.A., Drange, H., Elverhøi, A., Otterå, O.H., Solheim, A., 2002. Modelling Late Cenozoic isostatic elevation changes in the Barents Sea and their implications for oceanic and climatic regimes: preliminary results. *Quat. Sci. Rev.* 21 (14), 1643–1660. [https://doi.org/10.1016/S0277-3791\(02\)00018-5](https://doi.org/10.1016/S0277-3791(02)00018-5).
- Cartwright, J., James, D., Bolton, A., 2003. The genesis of polygonal fault systems: a review. *Geol. Soc. Lond., Spec. Publ.* 216 (1), 223–243. <https://doi.org/10.1144/GSL.SP.2003.216.01.15>.
- Chamley, H., 2001. Clay mineralogy*. In: Steele, J.H. (Ed.), *Encyclopedia of Ocean Sciences*, Second edition. Academic Press, Oxford, pp. 563–571. <https://doi.org/10.1016/B978-012374473-9.00186-7>.
- Clark, D.L., Hanson, A., 1983. Central Arctic Ocean sediment texture: a key to ice transport mechanisms. In: Molnia, B.F. (Ed.), *Glacial-Marine Sedimentation*. Springer US, Boston, MA, pp. 301–330. https://doi.org/10.1007/978-1-4613-3793-5_7.
- Clotten, C., et al., 2019. On the causes of Arctic Sea ice in the warm early Pliocene. *Sci. Rep.* 9 (1), 989. <https://doi.org/10.1038/s41598-018-37047-y>.

- De Schepper, S., Head, M.J., 2008. Age calibration of dinoflagellate cyst and acritarch events in the Pliocene-Pleistocene of the eastern North Atlantic (DSDP Hole 610A). *Stratigraphy* 5 (2), 137–161.
- De Schepper, S., Mangerud, G., 2018. Age and palaeoenvironment of the Utsira Formation in the northern North Sea based on marine palynology. *Nor. J. Geol.* 97, 305–325. <https://doi.org/10.17850/njg97-4-04>.
- De Schepper, S., Head, M.J., Groeneveld, J., 2009. North Atlantic current variability through marine isotope stage M2 (circa 3.3 Ma) during the mid-Pliocene. *Paleoceanography* 24, PA4206. <https://doi.org/10.1029/2008PA001725>.
- De Schepper, S., et al., 2013. Northern Hemisphere Glaciation during the Globally warm early late Pliocene. *PLoS One* 8 (12), e81508. <https://doi.org/10.1371/journal.pone.0081508>.
- De Schepper, S., et al., 2015. Early Pliocene onset of modern Nordic Seas circulation related to ocean gateway changes. *Nat. Commun.* 6, 8659. <https://doi.org/10.1038/ncomms9659>.
- De Schepper, S., Beck, K.M., Mangerud, G., 2017. Late Neogene dinoflagellate cyst and acritarch biostratigraphy for Ocean Drilling Program Hole 642B, Norwegian Sea. *Rev. Palaeobot. Palynol.* 236, 12–32. <https://doi.org/10.1016/j.revpalbo.2016.08.005>.
- Dörr, N., Lisker, F., Piepjohn, K., Spiegel, C., 2019. Cenozoic development of northern Svalbard based on thermochronological data. *Terra Nova* 31 (3), 306–315. <https://doi.org/10.1111/ter.12402>.
- Dossing, A., et al., 2016. Miocene uplift of the NE Greenland margin linked to plate tectonics: Seismic evidence from the Greenland Fracture Zone, NE Atlantic. *Tectonics* 35 (2), 257–282. <https://doi.org/10.1002/2015TC004079>.
- Dumais, M.A., Gernigon, L., Olesen, O., Johansen, S.E., Brönnner, M., 2021. New interpretation of the spreading evolution of the Knipovich Ridge derived from aeromagnetic data. *Geophys. J. Int.* 224 (2), 1422–1428. <https://doi.org/10.1093/gji/ggaa527>.
- Ehlers, B.-M., Jokat, W., 2009. Subsidence and crustal roughness of ultra-slow spreading ridges in the northern North Atlantic and the Arctic Ocean. *Geophys. J. Int.* 177 (2), 451–462. <https://doi.org/10.1111/j.1365-246X.2009.04078.x>.
- Ehlers, B.-M., Jokat, W., 2013. Paleo-bathymetry of the northern North Atlantic and consequences for the opening of the Fram Strait. *Mar. Geophys. Res.* 34 (1), 25–43. <https://doi.org/10.1007/s11001-013-9165-9>.
- Eiken, O., Hinz, K., 1993. Contourites in the Fram Strait. *Sediment. Geol.* 82 (1), 15–32. [https://doi.org/10.1016/0037-0738\(93\)90110-Q](https://doi.org/10.1016/0037-0738(93)90110-Q).
- Elderfield, H., et al., 2012. Evolution of ocean temperature and Ice volume through the mid-pleistocene climate transition. *Science* 337 (6095), 704–709. <https://doi.org/10.1126/science.1221294>.
- Eldrett, J.S., Harding, I.C., Wilshaw, R., Xuan, C., 2019. A new high northern latitude dinocyst-based magneto-biostratigraphic calibration for the Norwegian-Greenland Sea. *Newsl. Stratigr.* 52 (4), 435–460. <https://doi.org/10.1127/nos/2019/0496>.
- Engen, Ø., Faleide, J.I., Dyreng, T.K., 2008. Opening of the Fram Strait gateway: a review of plate tectonic constraints. *Tectonophysics* 450 (1), 51–69. <https://doi.org/10.1016/j.tecto.2008.01.002>.
- Engen, Ø., Gjengedal, J.A., Faleide, J.I., Kristoffersen, Y., Eldholm, O., 2009. Seismic stratigraphy and sediment thickness of the Nansen Basin, Arctic Ocean. *Geophys. J. Int.* 176 (3), 805–821. <https://doi.org/10.1111/j.1365-246X.2008.04028.x>.
- Faleide, J.I., et al., 1996. Late Cenozoic evolution of the western Barents Sea-Svalbard continental margin. *Glob. Planet. Chang.* 12 (1), 53–74. [https://doi.org/10.1016/0921-8181\(95\)00012-7](https://doi.org/10.1016/0921-8181(95)00012-7).
- Fensholt, R.A., Williams, G.L., Wood, S.E.L., Riding, J.B., 2019. A review of the areoligeracean dinoflagellate cyst Cyclonephelium and morphologically similar genera. *Palynology* 43 (sup1), 1–71. <https://doi.org/10.1080/01916122.2019.1596391>.
- Fiedler, A., Faleide, J.I., 1996. Cenozoic sedimentation along the southwestern Barents Sea margin in relation to uplift and erosion of the shelf. *Glob. Planet. Chang.* 12 (1), 75–93. [https://doi.org/10.1016/0921-8181\(95\)00013-5](https://doi.org/10.1016/0921-8181(95)00013-5).
- Fjeldskaar, W., Amantov, A., 2018. Effects of glaciations on sedimentary basins. *J. Geodyn.* 118, 66–81. <https://doi.org/10.1016/j.jog.2017.10.005>.
- Fronval, T., Jansen, E., 1996. Late neogene paleoclimates and paleoceanography in the iceland-Norwegian Sea: evidence from the iceland and Vøring Plateaus. In: Thiede, J., Myhre, A.M., Firth, J.V., Johnson, G.L., Ruddiman, W.F. (Eds.), *Proceedings of the Ocean Drilling Program, Scientific Results 151*. Texas A & M University, Ocean Drilling Program, College Station, TX, United States, pp. 455–468. <https://doi.org/10.2973/odp.proc.sr.151.134.1996>.
- Gebhardt, A.C., Geissler, W.H., Matthiessen, J., Jokat, W., 2014. Changes in current patterns in the Fram Strait at the Pliocene/Pleistocene boundary. *Quat. Sci. Rev.* 92 (0), 179–189. <https://doi.org/10.1016/j.quascirev.2013.07.015>.
- Geibert, W., Matthiessen, J., Stimac, I., Wollenburg, J., Stein, R., 2021. Glacial episodes of a freshwater Arctic Ocean covered by a thick ice shelf. *Nature* 590 (7844), 97–102. <https://doi.org/10.1038/s41586-021-03186-y>.
- Geissler, W.H., Jokat, W., 2004. A geophysical study of the northern Svalbard continental margin. *Geophys. J. Int.* 158 (1), 50–66. <https://doi.org/10.1111/j.1365-246X.2004.02315.x>.
- Geissler, W.H., Jokat, W., Brekke, H., 2011. The Yermak Plateau in the Arctic Ocean in the light of reflection seismic data-implication for its tectonic and sedimentary evolution. *Geophys. J. Int.* 187 (3), 1334–1362. <https://doi.org/10.1111/j.1365-246X.2011.05197.x>.
- Gladenkov, A.Y., Oleinik, A.E., Marinovich, L., Barinov, K.B., 2002. A refined age for the earliest opening of Bering Strait. *Palaeogeogr. Palaeoclimatol. Palaeoecol.* 183 (3), 321–328. [https://doi.org/10.1016/S0031-0182\(02\)00249-3](https://doi.org/10.1016/S0031-0182(02)00249-3).
- Gradstein, F.M., Ogg, J.G., Schmitz, M.D., Ogg, G.M., 2020. *Geologic Time Scale 2020*. Elsevier, p. 1390. <https://doi.org/10.1016/C2020-1-02369-3>.
- Green, P.F., Duddy, I.R., 2010. Synchronous exhumation events around the Arctic including examples from Barents Sea and Alaska North Slope. *Geol. Soc. London, Petrol. Geol. Conf. Series* 7 (1), 633. <https://doi.org/10.1144/0070633>.
- Gruetzner, J., Bassinot, F.C., Mienert, J., 1997. High resolution compressional wave velocity measurements in Pleistocene sediments of the Ceara Rise (western equatorial Atlantic): implications for orbital driven sedimentary cycles. In: Shackleton, N.J., Curry, W.B., Richter, C., Bralower, T.J. (Eds.), *Proceedings of the Ocean Drilling Program, Scientific Results 154*. Texas A & M University, Ocean Drilling Program, College Station, TX, United States, pp. 135–149. <https://doi.org/10.2973/odp.proc.sr.154.130.1997>.
- Gruetzner, J., et al., 2019. A New Seismic Stratigraphy in the Indian-Atlantic Ocean Gateway Resembles Major Paleo-Oceanographic changes of the last 7 Ma. *Geochem. Geophys. Geosyst.* 20 (1), 339–358. <https://doi.org/10.1029/2018GC007668>.
- Harishidayat, D., Johansen, S.E., Batchelor, C., Omosanya, K.O., Ottaviani, L., 2021. Pliocene–Pleistocene glacial-marine shelf to slope processes in the south-western Barents Sea. *Basin Res.* 33 (2), 1315–1336. <https://doi.org/10.1111/bre.12516>.
- Haug, G.H., Tiedemann, R., 1998. Effect of the formation of the Isthmus of Panama on Atlantic Ocean thermohaline circulation. *Nature* 393 (6686), 673–676. <https://doi.org/10.1038/31447>.
- Hayashi, T., et al., 2020. Latest Pliocene Northern Hemisphere glaciation amplified by intensified Atlantic meridional overturning circulation. *Commun. Earth Environ.* 1 (1), 25. <https://doi.org/10.1038/s43247-020-00023-4>.
- Hegewald, A., Jokat, W., 2013. Relative Sea level variations in the Chukchi region - Arctic Ocean - since the late Eocene. *Geophys. Res. Lett.* 40 (5), 803–807. <https://doi.org/10.1002/grl.50182>.
- Helland, P.E., Holmes, M.A., 1997. Surface textural analysis of quartz sand grains from ODP Site 918 off the southeast coast of Greenland suggests glaciation of southern Greenland at 11 Ma. *Palaeogeogr. Palaeoclimatol. Palaeoecol.* 135 (1), 109–121. [https://doi.org/10.1016/S0031-0182\(97\)00025-4](https://doi.org/10.1016/S0031-0182(97)00025-4).
- Herbert, T.D., et al., 2016. Late Miocene global cooling and the rise of modern ecosystems. *Nat. Geosci.* 9 (11), 843–847. <https://doi.org/10.1038/ngeo2813>.
- Hjelstuen, B.O., Sejrup, H.P., 2021. Latitudinal variability in the Quaternary development of the Eurasian ice sheets—evidence from the marine domain. *Geology* 49 (3), 346–351. <https://doi.org/10.1130/G48106.1>.
- Hodell, D.A., Channell, J.E.T., 2016. Mode transitions in Northern Hemisphere glaciation: co-evolution of millennial and orbital variability in Quaternary climate. *Clim. Past* 12 (9), 1805–1828. <https://doi.org/10.5194/cp-12-1805-2016>.
- Hodell, D.A., Venz-Curtis, K.A., 2006. Late Neogene history of Deepwater ventilation in the Southern Ocean. *Geochem. Geophys. Geosyst.* 7 (9), Q09001. <https://doi.org/10.1029/2005GC001211>.
- Holbourn, A., Kuhnt, W., Clemens, S., Prell, W., Andersen, N., 2013. Middle to late Miocene stepwise climate cooling: evidence from a high-resolution deep water isotope curve spanning 8 million years. *Paleoceanography* 28 (4). <https://doi.org/10.1002/2013PA002538>, 2013PA002538.
- Hu, A., Meehl, G.A., Han, W., 2007. Role of the Bering Strait in the thermohaline circulation and abrupt climate change. *Geophys. Res. Lett.* 34 (5), L05704. <https://doi.org/10.1029/2006GL028906>.
- Hull, D.M., Osterman, L.E., Thiede, J., 1996. Biostratigraphic Synthesis of Leg 151, North Atlantic-Arctic Gateways. In: Thiede, J., Myhre, A.M., Firth, J.V., Johnson, G.L., Ruddiman, W.F. (Eds.), *Proceedings of the Ocean Drilling Program, Scientific Results 151*. Texas A & M University, Ocean Drilling Program, College Station, TX, United States, pp. 627–644. <https://doi.org/10.2973/odp.proc.sr.151.146.1996>.
- Hustoft, S., Bünz, S., Mienert, J., Chand, S., 2009. Gas hydrate reservoir and active methane-venting province in sediments on <20 Ma young oceanic crust in the Fram Strait, offshore NW-Svalbard. *Earth Planet. Sci. Lett.* 284 (1), 12–24. <https://doi.org/10.1016/j.epsl.2009.03.038>.
- Israelson, C., Spezzaferrri, S., 1998. Strontium-isotope stratigraphy from Sites 918 and 919. In: Saunders, A.D., Larsen, H.C., Wise, S.W. (Eds.), *Proceedings of the Ocean Drilling Program, Scientific Results 152*. Texas A & M University, Ocean Drilling Program, College Station, TX, United States, pp. 233–242. <https://doi.org/10.2973/odp.proc.sr.152.214.1998>.
- Jakobsson, M., et al., 2007. The early Miocene onset of a ventilated circulation regime in the Arctic Ocean. *Nature* 447 (7147), 986–990. <https://doi.org/10.1038/nature05924>.
- Jakobsson, M., et al., 2012. The international bathymetric chart of the Arctic Ocean (IBCAO) version 3.0. *Geophys. Res. Lett.* 39 (12), L12609. <https://doi.org/10.1029/2012GL052219>.
- Japsen, P., Green, P.F., Bonow, J.M., Nielsen, T.F.D., Chalmers, J.A., 2014. From volcanic plains to glaciated peaks: Burial, uplift and exhumation history of southern East Greenland after opening of the NE Atlantic. *Glob. Planet. Chang.* 116, 91–114. <https://doi.org/10.1016/j.gloplacha.2014.01.012>.
- Johnson, J.E., et al., 2015. Abiotic methane from ultraslow-spreading ridges can charge Arctic gas hydrates. *Geology* 43 (5), 371–374. <https://doi.org/10.1130/G36440.1>.
- Jokat, W., 2003. The expedition ARKTIS XVIII/2 of RV “Polarstern” in 2002. In: *Berichte Zur Polarforschung (Reports on Polar Research)*, 368. Alfred Wegener Institute for Polar and Marine Research, Bremerhaven, p. 63. https://doi.org/10.2312/BzPM_0449.2003.
- Jokat, W., Lehmann, P., Damaske, D., Bradley Nelson, J., 2016. Magnetic signature of North-East Greenland, the Morris Jesup rise, the Yermak Plateau, the central Fram Strait: Constraints for the rift/drift history between Greenland and Svalbard since the Eocene. *Tectonophysics* 691, 98–109. <https://doi.org/10.1016/j.tecto.2015.12.002>.
- Kaminski, M.A., Silye, L.R.N., Kender, S., 2006. Miocene deep-water agglutinated foraminifera from ODP Hole 909c: implications for the paleoceanography of the Fram Strait Area, Greenland Sea. *Micropaleontology* 51 (5), 373–403. <https://doi.org/10.2113/gsmicropal.51.5.373>.

- Karas, C., et al., 2020. Did North Atlantic cooling and freshening from 3.65–3.5 Ma precondition Northern Hemisphere ice sheet growth? *Glob. Planet. Chang.* 185, 103085 <https://doi.org/10.1016/j.gloplacha.2019.103085>.
- Khélfifi, N., Frank, M., 2014. A major change in North Atlantic deep water circulation 1.6 million years ago. *Clim. Past* 10 (4), 1441–1451. <https://doi.org/10.5194/cp-10-1441-2014>.
- Kirilova, V., Osborne, A.H., Störing, T., Frank, M., 2019. Miocene restriction of the Pacific-North Atlantic throughflow strengthened Atlantic overturning circulation. *Nat. Commun.* 10 (1), 4025. <https://doi.org/10.1038/s41467-019-12034-7>.
- Kleiven, H.F., Jansen, E., Fronval, T., Smith, T.M., 2002. Intensification of Northern Hemisphere glaciations in the circum Atlantic region (3.5–2.4 Ma) – ice-rafted detritus evidence. *Palaeogeogr. Palaeoclimatol. Palaeoecol.* 184 (3), 213–223. [https://doi.org/10.1016/S0031-0182\(01\)00407-2](https://doi.org/10.1016/S0031-0182(01)00407-2).
- Knies, J., Gaina, C., 2008. Middle Miocene ice sheet expansion in the Arctic: views from the Barents Sea. *Geochim. Geophys. Geosyst.* 9 (2), Q02015. <https://doi.org/10.1029/2007GC001824>.
- Knies, J., Mann, U., 2002. Depositional environment and source rock potential of Miocene strata from the central Fram Strait: introduction of a new computing tool for simulating organic facies variations. *Mar. Pet. Geol.* 19 (7), 811–828. [https://doi.org/10.1016/S0264-8172\(02\)00090-9](https://doi.org/10.1016/S0264-8172(02)00090-9).
- Knies, J., Matthiessen, J., Vogt, C., Stein, R., 2002. Evidence of ‘Mid-Pliocene (3 Ma) global warmth’ in the eastern Arctic Ocean and implications for the Svalbard/Barents Sea ice sheet during the late Pliocene and early Pleistocene (3–1.7 Ma). *Boreas* 31 (1), 82–93. <https://doi.org/10.1111/j.1502-3885.2002.tb01058.x>.
- Knies, J., et al., 2009. The Plio-Pleistocene glaciation of the Barents Sea-Svalbard region: a new model based on revised chronostratigraphy. *Quat. Sci. Rev.* 28 (9–10), 812–829. <https://doi.org/10.1016/j.quascirev.2008.12.002>.
- Knies, J., et al., 2014. Effect of early Pliocene uplift on late Pliocene cooling in the Arctic–Atlantic gateway. *Earth Planet. Sci. Lett.* 387, 132–144. <https://doi.org/10.1016/j.epsl.2013.11.007>.
- Laberg, J.S., Andreassen, K., Vorren, T.O., 2012. Late Cenozoic erosion of the high-latitude southwestern Barents Sea shelf revisited. *GSA Bull.* 124 (1–2), 77–88. <https://doi.org/10.1130/B30340.1>.
- Lasabuda, A., et al., 2018. Late Cenozoic Erosion Estimates for the Northern Barents Sea: quantifying glacial sediment input to the Arctic Ocean. *Geochim. Geophys. Geosyst.* 19 (12), 4876–4903. <https://doi.org/10.1029/2018GC007882>.
- Lear, C.H., Rosenthal, Y., Wright, J.D., 2003. The closing of a seaway: ocean water masses and global climate change. *Earth Planet. Sci. Lett.* 210 (3–4), 425–436. [https://doi.org/10.1016/S0012-821X\(03\)00164-X](https://doi.org/10.1016/S0012-821X(03)00164-X).
- Louwye, S., De Schepper, S., 2010. The Miocene–Pliocene hiatus in the southern North Sea Basin (northern Belgium) revealed by dinoflagellate cysts. *Geol. Mag.* 147 (5), 760–776. <https://doi.org/10.1017/S0016756810000191>.
- Louwye, S., De Schepper, S., Laga, P., Vandenberghe, N., 2007. The Upper Miocene of the southern North Sea Basin (northern Belgium): a palaeoenvironmental and stratigraphical reconstruction using dinoflagellate cysts. *Geol. Mag.* 144 (1), 33–52. <https://doi.org/10.1017/S0016756806002627>.
- Lunt, D.J., Valdes, P.J., Haywood, A., Rutt, I.C., 2008. Closure of the Panama Seaway during the Pliocene: implications for climate and Northern Hemisphere glaciation. *Clim. Dyn.* 30 (1), 1–18. <https://doi.org/10.1007/s00382-007-0265-6>.
- Lyle, M., Bristow, J., Bloemendal, J., Rack, F.R., 1996. Comparison of natural gamma ray activity profiles from downhole logging and the MST core logger at Site 911 (Yermak Plateau). In: Thiede, J., Myhre, A.M., Firth, J.V., Johnson, G.L., Ruddiman, W.F. (Eds.), *Proceedings of the Ocean Drilling Program, Scientific Results*, 151. Texas A & M University, Ocean Drilling Program, College Station, TX, United States, pp. 369–376. <https://doi.org/10.2973/odp.proc.sr.151.125.1996>.
- Maslin, M.A., Brierley, C.M., 2015. The role of orbital forcing in the early Middle Pleistocene transition. *Quat. Int.* 389, 47–55. <https://doi.org/10.1016/j.quaint.2015.01.047>.
- Matthiessen, J., Brinkhuis, H., Poulsen, N., Smelror, M., 2009a. Decahedrella martinheadii Manum 1997 - A stratigraphically and paleoenvironmentally useful Miocene acritarch of the high northern latitudes. *Micropaleontology* 55 (2/3), 171–186.
- Matthiessen, J., Knies, J., Vogt, C., Stein, R., 2009b. Pliocene palaeoceanography of the Arctic Ocean and subarctic seas. *Philos. Trans. Royal Soc. Math. Phys. Eng. Sci.* 367 (1886), 21–48. <https://doi.org/10.1098/rsta.2008.0203>.
- Mattingsdal, R., et al., 2014. A new 6 Myr stratigraphic framework for the Atlantic–Arctic Gateway. *Quat. Sci. Rev.* 92, 170–178. <https://doi.org/10.1016/j.quascirev.2013.08.022>.
- Miller, K.G., et al., 2020. Cenozoic Sea-level and cryospheric evolution from deep-sea geochemical and continental margin records. *Sci. Adv.* 6 (20), eaaz1346 <https://doi.org/10.1126/sciadv.aaz1346>.
- Minakov, A., 2018. Late Cenozoic lithosphere dynamics in Svalbard: interplay of glaciation, seafloor spreading and mantle convection. *J. Geodyn.* 122, 1–16. <https://doi.org/10.1016/j.jog.2018.09.009>.
- Morton, R.W., 1975. Sound velocity in carbonate sediments from the Whiting Basin, Puerto Rico. *Mar. Geol.* 19 (1), 1–17. [https://doi.org/10.1016/0025-3227\(75\)90002-X](https://doi.org/10.1016/0025-3227(75)90002-X).
- Müller, R.D., Sdrolias, M., Gaina, C., Roest, W.R., 2008. Age, spreading rates, and spreading asymmetry of the world’s ocean crust. *Geochim. Geophys. Geosyst.* 9 (4), Q04006. <https://doi.org/10.1029/2007GC001743>.
- Myhre, A.M., Eldholm, O., Sundvor, E., 1982. The margin between Senja and Spitsbergen fracture zones: Implications from plate tectonics. *Tectonophysics* 89 (1), 33–50. [https://doi.org/10.1016/0040-1951\(82\)90033-6](https://doi.org/10.1016/0040-1951(82)90033-6).
- Myhre, A.M., et al., 1995a. Site 908. Site 908. In: Myhre, A.M., Thiede, J., Firth, J.V., et al. (Eds.), *Proceedings of the Ocean Drilling Program, Initial Reports* 151. Texas A & M University, Ocean Drilling Program, College Station, TX, United States, pp. 114–158. <https://doi.org/10.2973/odp.proc.ir.151.106.1995>.
- Myhre, A.M., et al., 1995b. Site 909. In: Myhre, A.M., Thiede, J., Firth, J.V., et al. (Eds.), *Proceedings of the Ocean Drilling Program, Initial Reports* 151. Texas A & M University, Ocean Drilling Program, College Station, TX, United States, pp. 159–220. <https://doi.org/10.2973/odp.proc.ir.151.107.1995>.
- Nielsen, T., Andersen, C., Knutz, P., Kuijpers, A., 2011. The Middle Miocene to Recent Davis Strait Drift Complex: implications for Arctic–Atlantic water exchange. *Geom. Mar. Lett.* 31 (5), 419–426. <https://doi.org/10.1007/s00367-011-0245-z>.
- O’Connell, S., Wolf-Welling, T.C.W., Cremer, M., Stein, R., 1996. Neogene paleoceanography and paleoclimate history from Fram Strait: changes in Accumulation Rates. In: Thiede, J., Myhre, A.M., Firth, J.V., Johnson, G.L., Ruddiman, W.F. (Eds.), *Proceedings of the Ocean Drilling Program, Scientific Results* 151. Texas A & M University, Ocean Drilling Program, College Station, TX, United States, pp. 569–582. <https://doi.org/10.2973/odp.proc.sr.151.140.1996>.
- Ogg, J.G., 2020. Chapter 5 - Geomagnetic Polarity Time Scale. In: Gradstein, F.M., Ogg, J.G., Schmitz, M.D., Ogg, G.M. (Eds.), *Geologic Time Scale 2020*. Elsevier, pp. 159–192. <https://doi.org/10.1016/B978-0-12-824360-2.00005-X>.
- Orvik, K.A., Niiler, P., 2002. Major pathways of Atlantic water in the northern North Atlantic and Nordic Seas toward Arctic. *Geophys. Res. Lett.* 29 (19), 1896. <https://doi.org/10.1029/2002GL015002>.
- Østerhus, S., Turrell, W.R., Jónsson, S., Hansen, B., 2005. Measured volume, heat, and salt fluxes from the Atlantic to the Arctic Mediterranean. *Geophys. Res. Lett.* 32 (7), L07603. <https://doi.org/10.1029/2004GL022188>.
- Pena, L.D., Goldstein, S.L., 2014. Thermohaline circulation crisis and impacts during the mid-Pleistocene transition. *Science* 345 (6194), 318–322. <https://doi.org/10.1126/science.1249770>.
- Pérez, L.F., Nielsen, T., Knutz, P.C., Kuijpers, A., Damm, V., 2018. Large-scale evolution of the central-East Greenland margin: New insights to the North Atlantic glaciation history. *Glob. Planet. Chang.* 163, 141–157. <https://doi.org/10.1016/j.gloplacha.2017.12.010>.
- Poirier, A., Hillaire-Marcel, C., 2011. Improved Os-isotope stratigraphy of the Arctic Ocean. *Geophys. Res. Lett.* 38 (14), L14607. <https://doi.org/10.1029/2011GL047953>.
- Poore, H.R., Samworth, R., White, N.J., Jones, S.M., McCave, I.N., 2006. Neogene overflow of Northern Component Water at the Greenland-Scotland Ridge. *Geochim. Geophys. Geosyst.* 7, Q06010. <https://doi.org/10.1029/2005GC001085>.
- Posamentier, H.W., Martinsen, O.J., 2011. The character and genesis of submarine mass-transport deposits: insights from outcrop and 3D seismic data. In: Shipp, R.C., Weimer, P., Posamentier, H.W. (Eds.), *Mass-Transport Deposits in Deepwater Settings*. SEPM Society for Sedimentary Geology, pp. 7–39. <https://doi.org/10.2110/sepm.sp.096.007>.
- Poulsen, N.E., Manum, S.B., Williams, G.L., Ellegaard, M., 1996. Tertiary Dinoflagellate Biostratigraphy of Sites 907, 908, and 909 in the Norwegian-Greenland Sea. In: Thiede, J., Myhre, A.M., Firth, J.V., Johnson, G.L., Ruddiman, W.F. (Eds.), *Proceedings of the Ocean Drilling Program, Scientific Results* 151. Texas A & M University, Ocean Drilling Program, College Station, TX, United States, pp. 255–285. <https://doi.org/10.2973/odp.proc.sr.151.110.1996>.
- Quaijtaal, W., Teseur, S., Donders, T.H., Claeys, P., Louwye, S., 2018. A revised and improved age model for the middle Miocene part of IODP Site U1318 (Porcupine Basin, offshore southwestern Ireland). *Geol. Mag.* 155 (5), 1105–1116. <https://doi.org/10.1017/S0016756816001278>.
- Rebesco, M., et al., 2013. Quaternary contourite drifts of the Western Spitsbergen margin. *Deep-Sea Res. I Oceanogr. Res. Pap.* 79, 156–168. <https://doi.org/10.1016/j.jdsr.2013.05.013>.
- Rebesco, M., Hernández-Molina, F.J., Van Rooij, D., Wåhlin, A., 2014a. Contourites and associated sediments controlled by deep-water circulation processes: State-of-the-art and future considerations. *Mar. Geol.* 352 (0), 111–154. <https://doi.org/10.1016/j.margeo.2014.03.011>.
- Rebesco, M., et al., 2014b. Onset and growth of Trough-Mouth Fans on the North-Western Barents Sea margin – implications for the evolution of the Barents Sea/Svalbard Ice Sheet. *Quat. Sci. Rev.* 92, 227–234. <https://doi.org/10.1016/j.quascirev.2013.08.015>.
- Ritzmann, O., et al., 2004. A deep seismic transect from Hovgård Ridge to northwestern Svalbard across the continental-ocean transition: a sheared margin study. *Geophys. J. Int.* 157 (2), 683–702. <https://doi.org/10.1111/j.1365-246X.2004.02204.x>.
- Rudels, B., et al., 2015. Circulation and transformation of Atlantic water in the Eurasian Basin and the contribution of the Fram Strait inflow branch to the Arctic Ocean heat budget. *Prog. Oceanogr.* 132, 128–152. <https://doi.org/10.1016/j.pocean.2014.04.003>.
- Rydningen, T.A., et al., 2020. An Early Neogene—Early Quaternary Contourite Drift System on the SW Barents Sea Continental Margin, Norwegian Arctic. *Geochim. Geophys. Geosyst.* 21 (11), e2020GC009142 <https://doi.org/10.1029/2020GC009142>.
- Saloranta, T.M., Haugan, P.M., 2001. Interannual variability in the hydrography of Atlantic water northwest of Svalbard. *J. Geophys. Res. Oceans* 106 (C7), 13931–13943. <https://doi.org/10.1029/2000JC000478>.
- Sangiorgi, F., Quaijtaal, W., Donders, T.H., Schouten, S., Louwye, S., 2021. Middle Miocene Temperature and Productivity Evolution at a Northeast Atlantic Shelf Site (IODP U1318, Porcupine Basin): Global and Regional Changes. *Paleoceanogr. Paleoclimatol.* 36 (7), e2020PA004059 <https://doi.org/10.1029/2020PA004059>.
- Schauer, U., Fahrbach, E., Østerhus, S., Rohardt, G., 2004. Arctic warming through the Fram Strait: Oceanic heat transport from 3 years of measurements. *J. Geophys. Res. Oceans* 109 (C6), C06026. <https://doi.org/10.1029/2003JC001823>.
- Schreck, M., Matthiessen, J., Head, M.J., 2012. A magnetostratigraphic calibration of Middle Miocene through Pliocene dinoflagellate cyst and acritarch events in the

- Iceland Sea (Ocean Drilling Program Hole 907A). *Rev. Palaeobot. Palynol.* 187, 66–94. <https://doi.org/10.1016/j.revpalbo.2012.08.006>.
- Schreck, M., Meheust, M., Stein, R., Matthiessen, J., 2013. Response of marine palynomorphs to Neogene climate cooling in the Iceland Sea (ODP Hole 907A). *Mar. Micropaleontol.* 101, 49–67. <https://doi.org/10.1016/j.marmicro.2013.03.003>.
- Senger, K., Tveranger, J., Ogata, K., Braathen, A., Planke, S., 2014. Late Mesozoic magmatism in Svalbard: a review. *Earth Sci. Rev.* 139, 123–144. <https://doi.org/10.1016/j.earscirev.2014.09.002>.
- Serreze, M.C., Barry, R.G., 2011. Processes and impacts of Arctic amplification: a research synthesis. *Glob. Planet. Chang.* 77 (1), 85–96. <https://doi.org/10.1016/j.gloplacha.2011.03.004>.
- Seton, M., et al., 2020. A global data set of present-day oceanic crustal age and seafloor spreading parameters. *Geochem. Geophys. Geosyst.* 21 (10), e2020GC009214 <https://doi.org/10.1029/2020GC009214>.
- Solgaard, A.M., Bonow, J.M., Langen, P.L., Japsen, P., Hvidberg, C.S., 2013. Mountain building and the initiation of the Greenland Ice Sheet. *Palaeogeogr. Palaeoclimatol. Palaeoecol.* 392 (0), 161–176. <https://doi.org/10.1016/j.palaeo.2013.09.019>.
- Solheim, A., Andersen, E.S., Elverhøi, A., Fiedler, A., 1996. Late Cenozoic depositional history of the western Svalbard continental shelf, controlled by subsidence and climate. *Glob. Planet. Chang.* 12 (1), 135–148. [https://doi.org/10.1016/0921-8181\(95\)00016-X](https://doi.org/10.1016/0921-8181(95)00016-X).
- Solheim, A., et al., 1998. Late Cenozoic seismic stratigraphy and glacial geological development of the East Greenland and Svalbard-Barents Sea continental margins. *Quat. Sci. Rev.* 17 (1), 155–184. [https://doi.org/10.1016/S0277-3791\(97\)00068-1](https://doi.org/10.1016/S0277-3791(97)00068-1).
- Soliman, A., Ćorić, S., Head, M.J., Piller, W.E., El Beialy, S.Y., 2012. Lower and Middle Miocene biostratigraphy, Gulf of Suez, Egypt based on dinoflagellate cysts and calcareous nannofossils. *Palynology* 36 (1), 38–79. <https://doi.org/10.1080/01916122.2011.633632>.
- Spiegler, D., 1996. Planktonic foraminifer cenozoic biostratigraphy of the Arctic Ocean, Fram Strait (Sites 908–909), Yermak Plateau (Sites 910–912), and East Greenland Margin (Site 913). In: Thiede, J., Myhre, A.M., Firth, J.V., Johnson, G.L., Ruddiman, W.F. (Eds.), *Proceedings of the Ocean Drilling Program, Scientific Results 151*. Texas A & M University, Ocean Drilling Program, College Station, TX, United States, pp. 153–167. <https://doi.org/10.2973/odp.proc.sr.151.102.1996>.
- Stein, R., 2008. Chapter four proxies used for palaeoenvironmental reconstructions in the Arctic Ocean. In: Stein, R. (Ed.), *Developments in Marine Geology*. Elsevier, pp. 133–243. [https://doi.org/10.1016/S1572-5480\(08\)00004-3](https://doi.org/10.1016/S1572-5480(08)00004-3).
- Stein, R., 2019. The late Mesozoic-Cenozoic Arctic Ocean climate and Sea Ice history: a Challenge for past and Future Scientific Ocean Drilling. *Paleoceanogr. Paleoclimatol.* 34 (12), 1851–1894. <https://doi.org/10.1029/2018PA003433>.
- Steinthorsdottir, M., et al., 2021. The Miocene: the future of the past. *Paleoceanogr. Paleoclimatol.* 36 (4), e2020PA004037 <https://doi.org/10.1029/2020PA004037>.
- Stockmarr, J., 1971. Tablets with spores used in absolute pollen analysis. *Pollen Spores* 13, 615–621.
- Straume, E.O., et al., 2019. GlobSed: Updated Total Sediment Thickness in the World's Oceans. *Geochem. Geophys. Geosyst.* 20 (4), 1756–1772. <https://doi.org/10.1029/2018GC008115>.
- Straume, E.O., Gaina, C., Medvedev, S., Nisancioglu, K.H., 2020. Global Cenozoic Paleobathymetry with a focus on the Northern Hemisphere Oceanic Gateways. *Gondwana Res.* 86, 126–143. <https://doi.org/10.1016/j.gr.2020.05.011>.
- Talwani, M., Eldholm, O., 1977. Evolution of the Norwegian-Greenland Sea. *GSA Bull.* 88 (7), 969–999. [https://doi.org/10.1130/0016-7606\(1977\)88<969:EOTNS>2.0.CO;2](https://doi.org/10.1130/0016-7606(1977)88<969:EOTNS>2.0.CO;2).
- Thiede, J., et al., 1998. Late Cenozoic history of the polar North Atlantic: results from ocean drilling. *Quat. Sci. Rev.* 17 (1), 185–208. [https://doi.org/10.1016/S0277-3791\(97\)00076-0](https://doi.org/10.1016/S0277-3791(97)00076-0).
- Uenzelmann-Neben, G., Gruetzner, J., 2018. Chronology of Greenland Scotland Ridge overflow: what do we really know? *Mar. Geol.* 406, 109–118. <https://doi.org/10.1016/j.margeo.2018.09.008>.
- Venz, K.A., Hodell, D.A., 2002. New evidence for changes in Plio-Pleistocene deep water circulation from Southern Ocean ODP Leg 177 Site 1090. *Palaeogeogr. Palaeoclimatol. Palaeoecol.* 182 (3–4), 197–220. [https://doi.org/10.1016/S0031-0182\(01\)00496-5](https://doi.org/10.1016/S0031-0182(01)00496-5).
- Verhoeven, K., Louwye, S., Eiríksson, J., De Schepper, S., 2011. A new age model for the Pliocene–Pleistocene Tjörnes section on Iceland: its implication for the timing of North Atlantic–Pacific palaeoceanographic pathways. *Palaeogeogr. Palaeoclimatol. Palaeoecol.* 309 (1), 33–52. <https://doi.org/10.1016/j.palaeo.2011.04.001>.
- Waghorn, K.A., Bünz, S., Plaza-Faverola, A., Johnson, J.E., 2018. 3-D seismic investigation of a gas hydrate and fluid flow system on an active Mid-Ocean Ridge; Svyatogor Ridge, Fram Strait. *Geochem. Geophys. Geosyst.* 19 (8), 2325–2341. <https://doi.org/10.1029/2018GC007482>.
- Wahsner, M., et al., 1999. Clay-mineral distribution in surface sediments of the Eurasian Arctic Ocean and continental margin as indicator for source areas and transport pathways — a synthesis. *Boreas* 28 (1), 215–233. <https://doi.org/10.1111/j.1502-3885.1999.tb00216.x>.
- Wei, W., 1998. Calcareous nannofossils from the Southeast Greenland margin: Biostratigraphy and paleoceanography. In: Saunders, A.D., Larsen, H.C., Wise, S.W. (Eds.), *Proceedings of the Ocean Drilling Program, Scientific Results 152*. Texas A & M University, Ocean Drilling Program, College Station, TX, United States, pp. 147–160. <https://doi.org/10.2973/odp.proc.sr.152.215.1998>.
- Westerhold, T., et al., 2020. An astronomically dated record of Earth's climate and its predictability over the last 66 million years. *Science* 369 (6509), 1383. <https://doi.org/10.1126/science.aba6853>.
- Winkler, A., Wolf-Welling, T., Statterger, K., Thiede, J., 2002. Clay mineral sedimentation in high northern latitude deep-sea basins since the Middle Miocene (ODP Leg 151, NAAG). *Int. J. Earth Sci.* 91 (1), 133–148. <https://doi.org/10.1007/s005310100199>.
- Wolf-Welling, T.C.W., Cremer, M., O'Connell, S., Winkler, A., Thiede, J., 1996. Cenozoic Arctic gateway paleoclimate variability; indications from changes in coarse-fraction composition. In: Thiede, J., Myhre, A.M., Firth, J.V., Johnson, G.L., Ruddiman, W.F. (Eds.), *Proceedings of the Ocean Drilling Program, Scientific Results 151*. Texas A & M University, Ocean Drilling Program, College Station, TX, United States, pp. 515–567. <https://doi.org/10.2973/odp.proc.sr.151.139.1996>.
- Wright, J.D., Miller, K.G., 1996. Control of North Atlantic Deep Water Circulation by the Greenland-Scotland Ridge. *Paleoceanography* 11 (2), 157–170. <https://doi.org/10.1029/95PA03696>.
- Zevenboom, D., 1995. *Dinoflagellate Cysts from the Mediterranean Late Oligocene and Miocene*. Ph. D. Thesis. Utrecht University, Utrecht, Netherlands, p. 221.
- Zieba, K., Omosanya, K., Knies, J., 2017. A flexural isostasy model for the Pleistocene evolution of the Barents Sea bathymetry. *Nor. Geol. Tidsskr.* 97, 1–19. <https://doi.org/10.17850/njg97-1-01>.